Universitat de València
DEPARTAMENT DE FÍSICA ATÒMICA
MOLECULAR I NUCLEAR

VNIVERSITAT DE VALÈNCIA

Top quark studies at a Linear Collider

TESIS DE MÁSTER
Ignacio García García
Septiembre de 2012

Abstract

The International Linear Collider (ILC) is a proposed e^+e^- collider with a center-of-mass energy of 500 GeV, aimed at precision measurements, e.g. of a light Higgs-like boson that has been discovered recently at the Large Hadron Collider. Its detectors require the use of fine grained calorimeters to achieve the desired precisions.

This thesis presents the study of top quark pair production at the ILC.

The semileptonic decay of the top quark is studied with a full simulation of the proposed detector for the ILC (called ILD) at center-of-mass energy $\sqrt{s} = 500$ GeV and integrated luminosity $\mathcal{L} = 500\ fb^{-1}$ (expected for a 4 years running).

The detector performance permits to reach efficiencies larger than 70% in finding top events with a purity larger than 95%. This translates into a relative accuracy of about 1% top forward-backward asymmetry A^t_{FB} with electrons(positrons) polarizations of 80%(30%).

The aim of this thesis is to obtain the errors of the top quark couplings to the Z and the γ bosons, using observables like A^t_{FB}, cross-sections (σ) or helicity angle (λ_{hel}).

Dr. EDUARDO ROS, Investigador científico del Consejo Superior de Investigaciones Científicas (CSIC),
Dr. MARCEL VOS, Ramón y Cajal-CSIC,

CERTIFICAMOS:

Que la presente memoria *Top quark studies at a Linear Collider* ha sido realizada bajo nuestra dirección en el Departamento de Física Atómica Molecular y Nuclear de la Universitat de València por Ignacio García García y constituye su Tesis de Máster de Física Avanzada.

Y para que así conste, firmamos el presente Certificado.

Firmado: Eduardo Ros

Firmado: Marcel Vos

Contents

Chapter 1

Introduction

The theories and discoveries of thousands of physicists over the past century have resulted in a remarkable insight into the fundamental structure of matter: everything in the Universe is found to be made from twelve basic building blocks called fundamental particles, governed by four fundamental forces. Our best understanding of how these twelve particles and three of the forces are related to each other is encapsulated in the Standard Model of particles and forces. The Standard Model describes the electromagnetic, weak and strong nuclear interactions. Developed in the early 1970s, it has successfully explained a host of experimental results and precisely predicted a wide variety of phenomena. Over time and through many experiments by many physicists, the Standard Model has become established as a well−tested physics theory.

The Higgs boson is one of the essential pieces of the Standard Model due to the Higgs field is the mechanism which elementary particles acquire mass. It has no spin, electric charge, or colour charge. It is also unstable, decaying into other particles like fermion pairs or gauge boson pairs.

More recently, on 4 July 2012, the CMS and the ATLAS experimental teams at the Large Hadron Collider independently announced that they confirmed the formal discovery of a previously unknown boson of mass between 125−127 GeV/c^2, whose behaviour so far has been "consistent with" a Higgs boson. Because of its success in explaining a wide variety of experimental results, the Standard Model is sometimes regarded as a "theory of almost everything", except gravity.

The International Linear Collider (ILC) is a proposed electron-positron collider aimed at precision measurements between center-of-mass energies of 90 GeV and 1 TeV. To achieve precision measurements, the design of detectors for the ILC is driven by the particle flow approach. Two important aspects were studied during this theses and constitute its results: the use and potential of the particle flow concept and precision measurements at the ILC.

The main part of this thesis will focus on analysis of the top quark production at the ILC using the semileptonic decay mode at a center-of-mass energy $\sqrt{s} = 500$ GeV with an integrated luminosity of $\mathcal{L} = 500\ fb^{-1}$ in 4 years. Emphasis will be put on the role of electron and positron polarization for precision physics.

1.1 The Standard Model of particle physics

Particle physics studies the components of matter and their interactions. They are described by the Standard Model (SM) [1] of particle physics illustrated Fig. 1.1. It is a relativistic quantum field theory using local gauge symmetries[1]. The electromagnetic, weak and strong interactions are all described within the SM. Gravitation is not included. The weakness of this interactions at the energies at which the SM is valid does not lead to measurable effects. Currently, there exists no satisfactory theory which includes gravity.

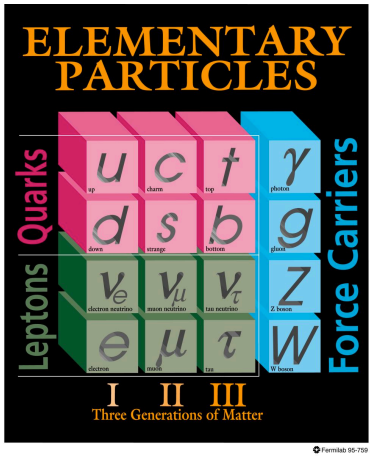

Figure 1.1: The Standard Model of particle physics. Fermions that build up matter are subdivided into three families of quarks and leptons. Vector bosons carry the strong, electromagnetic and weak forces. Picture taken from `http://www.fnal.gov/`.

1.1.1 Content of the SM

Spin 1/2 fermions are the building blocks of matter, divided in three families. They are organized in left-handed doublets and right-handed singlets under $SU(2)_L$ and charged under $U(1)_Y$ (where Y is the hypercharge). Leptons are color singlets while quarks are triplets under $SU(3)_c$ (c stands for color), the gauge group of the strong interaction. The electroweak group $SU(2)_L$ x $U(1)_Y$ is actually broken down to the electromagnetic group $U(1)_{em}$, giving the electric charge Q (in units of e) by:

$$Q = I_3^L + Y \tag{1.1}$$

where I_3^L is the third component of the $SU(2)_L$ isospin, with $I_3^L = \pm 1/2$ for left-handed fermions and $I_3^L = 0$ for right-handed fermions.

Spin 1 vector bosons mediate the interactions. The photon is massless and couples to electrically charged particles. The three bosons (Z^0 and $W^\pm$) mediate the weak force. There are 8 gluons associated to the strong interaction.

[1] In all the text, we will use natural units: $\hbar = c = 1$. Energies, masses and momenta will be expressed in GeV.

1.1.2 Electromagnetic interaction

Quantum Electrodynamics (QED) is the quantum field theory used for electromagnetic interactions using the $U(1)_{em}$ gauge group. The simplest associated Lagrangian for a massless fermion ψ with a massless photon field A_μ is:

$$\mathcal{L} = \bar{\psi}(i\gamma^\mu D_\mu)\psi - \frac{1}{4}F_{\mu\nu}F^{\mu\nu} \tag{1.2}$$

where $D_\mu = \partial_\mu - iQeA_\mu$ is the covariant derivative with Q the electric charge of ψ in units of e (Q = -1 for an electron). The gauge invariant kinetic term of the $\partial_\mu A_\nu - \partial_\nu A_\mu$ is the strength tensor of the photon field.
This Lagrangian is invariant under

$$\begin{cases} \psi \to \psi e^{iQe\chi(x)} \\ A_\mu \to A_\mu + \partial_\mu \chi \end{cases} \tag{1.3}$$

The strength of the electromagnetic interaction $\alpha = \frac{e^2}{4\pi\epsilon_0}$ is actually a running coupling constant depending on the tranferred foru-momentum squared, Q^2, in the reaction ($\alpha = 7.2973525376(50) \cdot 10^{-3} \approx \frac{1}{137}$ for zero exchanged momentum, and $\alpha(m_Z^2) \approx \frac{1}{128}$). Indeed, an electron can emit virtual photons which may convert into e^+e^- pairs (but also into pairs of quark-anti-quark and the other charged leptons) with the positrons being attracted by the electron. The charge of the electron is thus screened and a probe moving closer and closer to the electron (large Q^2) would feel an increasing charge when penetrating the positrons cloud.

1.1.3 Strong interaction

QCD Lagrangian Quantum chromodynamics (QCD) is the quantum field theory of strong interactions. The $SU(3)_c$ group is the relevant gauge group for three color charges. The gauge invariant Lagrangian of a massless quark q with fields of massless gluons G_μ^a (a = 1, ..., 8) reads:

$$\mathcal{L} = \bar{q}(i\gamma^\mu D_\mu)q - \frac{1}{4}G^a_{\mu\nu}G_a^{\mu\nu} \tag{1.4}$$

where $D_\mu = \partial_\mu - igT_aG_\mu^a$, with g coupling constant, $G^a_{\mu\nu} = \partial_\mu G^a_\nu - \partial_\nu G^a_\mu - gf_{abc}G^b_\mu G^c_\nu$ and T^a and f_{abc} are respectively the non-abelian group generators and the structure constants.

This group $SU(3)_c$ which is non-abelian leads to extra terms in the kinetic term of the gluon field which are triple and quadruple gluon couplings. These couplings are uniquely determined by the single coupling g.

Due to the number of colors and families, the running of the QCD strength $\alpha_s = \frac{g^2}{4\pi}(\alpha_s(m_Z^2) = 0.1184(7))$ leads to different behaviours from the QED constant α: α_s features an asymptotic freedom.

The asymptotic freedom implies that the force between quarks at short distances is small (large Q^2). But it is strong at larger distances (small Q^2), which prevents the existence of colored objects. A quark-anti-quark pair cannot separate because of this. Therefore quarks are only found in colourless combinations. However, if their

energy is large enough, as the potential energy between the quark and anti-quark increases with their distance, it becomes at a given point sufficicently large to create a pair of quark-anti-quark and so on. Quark-anti-quark pairs are produced until the energy is insufficient to continue the process. The final state partons combine into hadrons. This process is called hadronization. The particles resulting from the primary quark form a jet: a spray of hadrons produced by the hadronization of the initial parton.

1.1.4 Electroweak interactions

The model of weak interactions first proposed by Fermi was an effective theory, valid at energies well below 100GeV. The weak and electromagnetic interactions have been unified in the $SU(2)_L$ $U(1)_Y$ by Glashow in 1961 and the actual model was proposed by Weinberg and Salam. The weak interactions have a V-A (vector - axial vector) structure. In particular, the charged current only acts on left-handed fermions (right-handed anti-fermions).

Using $W^i_\mu (i = 1, 2, 3)$ for the vector fields of $SU(2)_L$ with coupling g and B_μ for the vector field of $U(1)_Y$ with coupling g, the basic electroweak interaction taken from the gauge covariant derivative applied on a fermion f can be written:

$$-ig(J^i)^\mu W^i_\mu - ig'(j^Y)^\mu B_\mu \tag{1.5}$$

The weak isospin current $J^i_\mu = \bar{f}\frac{\tau^i}{2}\gamma^\mu\frac{1-\gamma^5}{2}f$ only couples to left-handed fermions while $j^Y_\mu = \bar{f}Y\gamma_\mu f$ couples to all fermions charged under the hypercharge Y. The matrices τ^i (i = 1,2,3) are the Pauli matrices.

Using $\tau_\pm = \frac{1}{2}(\tau_1 + i\tau_2)$ and $W^\pm_\mu = \frac{W^1_\mu \mp iW^2_\mu}{\sqrt{2}}$, the charged part can be identified with a $\frac{g}{\sqrt{2}}$ coupling.

The weak neutral current is known to have a right-handed component, which suggests that there be a mixing between the neutral W^3_μ and B_μ bosons to embed weak and electromagnetic interactions arising from the breaking of the $SU(2)_L$ $U(1)_Y$ symmetry, down to $U(1)_{em}$. It is parametrized as:

$$\begin{aligned} A_\mu &= B_\mu cos\theta_W + W^3_\mu sin\theta_W \\ Z_\mu &= -B_\mu sin\theta_W + W^3_\mu cos\theta_W \end{aligned} \tag{1.6}$$

where A_μ and Z_μ are now the physical states of the photon and Z boson. θ_W is the Weinberg or weak mixing angle. Requiring that the photon current is that of QED ($-ie\bar{f}\gamma^\mu Qf$), one identifies the following relations:

$$\begin{aligned} \frac{g'}{g} &= tan\theta_W \\ e &= g' cos\theta_W \end{aligned} \tag{1.7}$$

and the couplings to Z_μ are:

$$\frac{e}{sin\theta_W cos\theta_W}(I^L_3 - Qsin^2\theta_W) \tag{1.8}$$

This form shows that the couplings are different from the pure left-handed couplings of $SU(2)_L$ because of the $Qsin^2\theta_W$ term that allows coupling of the Z with charged right-handed fermions.

1.2 The International Linear Collider

The LHC at CERN is now the most energetic collider ever built. It collides protons at energies in the center-of-mass of 7 TeV. Moreover LHC aims at discoveries of SUSY or other physics beyond the Standard Model.

It is a worldwide consensus that the next machine after the LHC must be a linear electron positron collider. It would complement the LHC by providing much more precise measurements and eventually additional discoveries. Currently the most advanced proposal is the International Linear Collider (ILC) which is described in the following. The worldwide efforts and ongoing R&D on the ILC are coordinated by the Global Design Effort (GDE). The major baseline of the ILC was documented in 2007 in a Reference Design Report[2]. The goal of the GDE is now to provide a Technical Design Report by the end of 2012 which will assess changes to the baseline in particular to better optimize the costs and performances. An alternative at higher center-of-mass energies than the ILC is the Compact Linear Collider (CLIC).

1.2.1 Physics cases for the ILC

Measuring the properties of a light Higgs boson or revealing other physics beyond the SM which must appear at an energy scale of about 1 TeV justifies the need for a precision machine in this energy range. Different scenarios of physics are envisaged for the ILC.[3]

The aim is to test the Higgs, but also top quark and W pairs to a precision which would require a linear collider. This can be done with an ILC operating at 500 GeV. In case there are other accompanying signals from SUSY or other theories, one would use this information to optimize accordingly the energy of a future linear collider.

In view of these possibilities, the ILC is designed at a nominal energy of 500GeV in the electron positron center-of-mass with symmetric momenta.

The machine can be upgraded up to $\sqrt{s} = 1$ TeV. Several other options are also proposed like GigaZ which consists in running at the Z pole to produce about 10^9 Z bosons in less than a year. Other options of e^-e^- collisions or $e\gamma$ and $\gamma\gamma$ collisions (by using an intense laser beam near the IP) are foreseen.

1.2.2 The Accelerator

The expected luminosity of the ILC is of 500 fb^{-1} at a center-of-mass energy of 500 GeV and in four years of running, while the design luminosity is $\mathcal{L} = 2\times10^{34}cm^{-2}s^{-1}$.

At high energies circular electron-positron machines become inefficient. Losses due to synchrotron radiation cannot be compensated anymore by reasonable means. The ILC is thus a 31 km-long linear electron-positron machine using superconductive accelerating cavities.

The principal systems are schematized Fig. 1.2, with the parameters given Table 1.1.

- A photocathode DC gun generates bunch trains of polarized electrons. The

Center-of-mass energy $\sqrt{s}$ (GeV)	200	230	250	350	500	upgrade 1,000
Collision rate f_{rep} (Hz)	5	5	5	5	5	4
Electron linac rate f_{linac} (Hz)	10	10	10	5	5	4
Number of bunches nb	1,312	1,312	1,312	1,312	1,312	2,625
Electron bunch population N- ($\times 10^{10}$)	2	2	2	2	2	2
Positron bunch population N+ ($\times 10^{10}$)	2	2	2	2	2	2
Main linac average gradient G_{av} (MV/m)	12.6	14.5	15.8	22.1	31.5	>31.5
RMS bunch length σ_{z} (mm)	0.3	0.3	0.3	0.3	0.3	0.3
Electron RMS energy spread $\Delta p/p$ (%)	0.22	0.22	0.22	0.22	0.21	0.11
Positron RMS energy spread $\Delta p/p$ (%)	0.17	0.15	0.14	0.1	0.07	0.04
Electron polarization P (%)	80	80	80	80	80	80
Positron polarization P' (%)	31	31	31	29	22	22
IP RMS horizontal beam size $\sigma_{\text{x}}*$ (nm)	904	843	700	662	474	554
(without traveling focus [Bal]) IP RMS vertical beam size $\sigma_{\text{y}}*$ (nm)	9.3	8.6	8.3	7	5.9	3.3
Luminosity $\mathcal{L} \times 10^{34}\, cm^{-2} s^{-1}$	0.47	0.54	0.71	0.86	1.49	2.7
Fraction of luminosity in top 1% $\mathcal{L}_{0.01}/\mathcal{L}$	92.20%	89.80%	84.10%	79.30%	62.50%	63.50%
Average energy loss δE_{BS}	0.61%	0.78%	1.23%	1.75%	4.30%	4.86%
(with traveling focus) IP RMS vertical beam size $\sigma_{\text{y}}*$ (nm)	6	5.6	5.3	4.5	3.8	2.7
Luminosity $\mathcal{L} \times 10^{34}\, cm^{-2} s^{-1}$	0.64	0.73	0.97	1.17	2.05	3.39
Fraction of luminosity in top 1% $\mathcal{L}_{0.01}/\mathcal{L}$	91.60%	89.00%	83.00%	77.90%	60.80%	62.30%
Average energy loss δE_{BS}	0.61%	0.79%	1.26%	1.78%	4.33%	4.85%

Table 1.1: Parameters of the ILC. The R&D is still ongoing and some figures may change.

polarization of the electrons is required to be greater than 80%. The electrons are accelerated up to 5 GeV and sent to the electron damping ring.

- The positrons are produced using already accelerated electrons. These electrons are extracted from the main linear accelerator (linac), deviated to an helical undulator and returned to the main linac with about 3 GeV lost, while high energy photons of approximately 10 MeV have been created and are targeted to create $e^- e^+$ pairs. The remaining photons and the created electrons are separated and then dumped. The positrons are accelerated to 5 GeV and enter their damping ring.

- Two damping rings with a circumference of 3.2 km will exist: one for electrons, one for positrons, where their spin is rotated perpendicular to the plane of the ring in order not to loose polarization. The aim is to reduce the transverse emittance of the bunches. Electrons and positrons need to be injected in the ring to main linac part of the accelerator without affecting the emittance and within the time between each train.

- Once electrons and positrons are extracted from the damping rings located near the center of the site, they need to be transported to the main linac. The ring to main linac system is thus used to inject the trains in the corresponding linac while rotating the spins to provide longitudinally polarized beams. It will also compress the bunch trains from several mm to a few hundred μm.

- The main linacs are 11 km long. The accelerating elements of the main linac are superconductive radio-frequency 1.3GHz cavities, as recommended by the

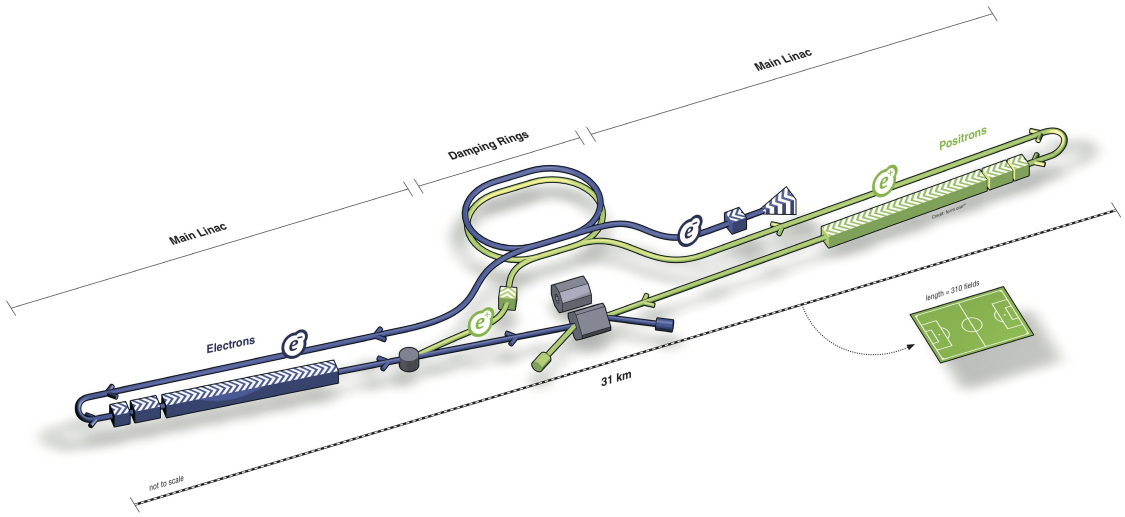

Figure 1.2: Layout of the ILC

International Technology Recommendation Panel in August 2004, cooled down to 2K. This is the primary cost driver of the project and an extensive and international R&D is made to produce these cavities. The basic element is a nine-cell 1.3 GHz niobium cavity, with an average accelerating gradient of 31.5 MV/m. To ensure this gradient for operations, a reproducible 35 MV/m gradient for these cavities must be demonstrated with a production yield greater than 90%. The beam spread must remain within approximately 0.1% at the interaction point (IP).

- Finally, the beams are collided with the beam delivery system (BDS). It is a 4.5 km-long system which focuses the beams at the IP to reach the designed luminosity with collisions at a 14 mrad crossing angle. In addition, it must extract the beams from the high energy linacs to protect the detectors. It should also provide means to monitor the beams before and after the interaction.

As for all previous colliders, there are strong motivations for having two detectors: competition and redundancy in the physics results, but also complementarity, in having different types of subdetectors. In addition, a failure of one of these very challenging detectors would not cause too long downtime. Two interaction zones had been envisaged by switching periodically the beams near the interaction region in two opposite points. But costs forced to keep only one IP. In an alternating fashion, two detectors will be moved into the interaction zone. To realize this push-pull scheme intensive engineering studies are ongoing.

1.2.3 Measuring beam polarization

Polarization is important in several physics cases. The polarimeters present in the baseline of the ILC should provide a 0.5% accuracy on the polarization of both beams before and after the IP but some processes even need it to be known with a better accuracy at the IP. To achieve this, a commonly used scheme is the "Blondel

scheme". W pair production ($e^+e^- \rightarrow W^+W^-$) is expected to be used with a modified version of the Blondel scheme, to measure the polarization of the beams with a 0.2% precision. It requires to provide regular helicity-sign flip of the beams.

Some improvements for the process ($e^+e^- \rightarrow W^+W^-$) can be foreseen. Its left-right polarization asymmetry is about 98.8% (see Table 8.1). Selecting small W polar angles (cos > 0.7), one reaches an almost 100% pure sample of left-handed W bosons, thus allowing to deduce the uncertainty on the effective polarization P_{eff} with 0.1% accuracy if only two configurations of polarization are used, those with opposite helicities of the beams. This could be valid even if the positrons are not polarised, as is the case in the baseline of the ILC.

Chapter 2

The ILD detector concept at the ILC

The ILD detector [4] *(Figure 2.1)* design is optimised for excellent jet energy resolution over a wide solid angle and for high-precision reconstruction of exclusive final states. A major goal in the design is the event reconstruction within the particle flow paradigm. The detector is relatively large to improve the separation between neutral particles, has a sizeable magnetic field to separate charged from neutral particles and to sweep away low-momentum backgrounds and is optimsed for highly efficient, precise particle reconstruction, in particular very robust, redundant pattern recognition of particles in the tracker and in the calorimeter.

The calorimeter plays a central role in the reconstruction of the complete event properties. A system of unprecedented granularity is proposed for ILD, both for the electromagnetic and the hadronic sections. the complete calorimeter is located inside the magnet. The flux from the coil is returned through an iron yoke, which is instrumented to serve as a muon filter in addition. It is complemented by a system of small, precise and radiation hard calorimeters in the very forward direction, used to complete the solid angle coverage, and to measure precisely the luminosity of the collider.

The tracker inside the calorimeter is a combination of a powerful large-volume time projection chamber (TPC) and an extensive silicon tracking system. The TPC provides up to 200 space points per particle, allowing efficient and highly redundant pattern recognition. It is combined with silicon tracking stations, both inside and outside of the TPC and covering the end plate, to provide addition high precision points. Located close to the beam pipe is a high-precision vertex detector.

2.1 ILD tracking

The ILD concept has chosen a combination of continuous tracking and discrete tracking, the former being a TPC central tracker and the latter being layers of silicon detectors. This combination has been chosen to provide a robust system with superb pattern recognition ability due to the large and redundant number of points provided and the complementary strength of silicon and gaseous tracking.

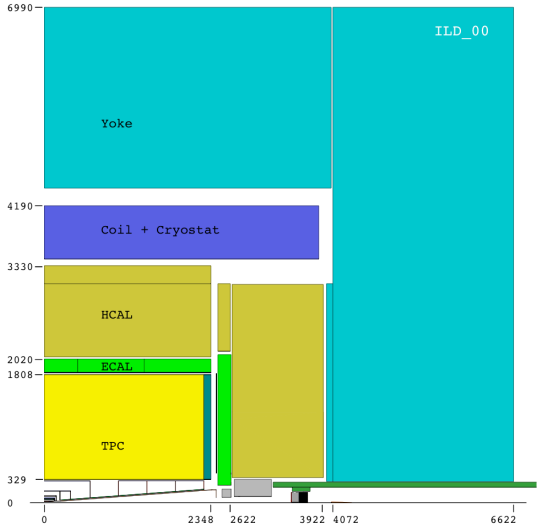

(a) Quadrant view of the ILD detector model.

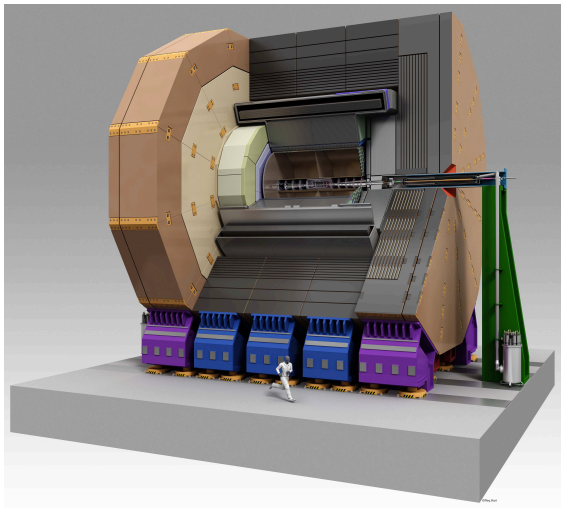

(b) 3D view

Figure 2.1: ILD detector. At the center, the interaction region surrounded by the tracking system. The ECAL and HCAL are placed inside the coil and the iron ensures the return of the magnetic field.

The interaction point is surrounded by a multi-layer pixel-vertex detector (VTX) followed by a system of strip and pixel detectors. In the barrel, two layers of silicon strip inner tracking detectors (SIT) are arranged to bridge the gap between the VTX and the TPC. In the forward region, a system of silicon pixel and silicon strip forward tracking disks (FTD) provides low angle tracking coverage[5].

A large volume TPC with up to 224 points per track provides continuous tracking for a large volume. The TPC is optimised for excellent three-dimensional point resolution and minimum material in the field cage and in the end plate. It also provides particle identification capabilities based on the energy loss of particles per unit of distance (dE/dx).

A system of Si-strip detectors provides additional high-precision space points, which improve the tracking measurements and provide additional redundancy in the regions between the main tracking volume and the calorimeters. It consists of the silicon internal tracker (SIT) between the vertex detector and TPC, and the silicon external tracker (SET) between the TPC and the electromagnetic calorimeter (ECAL) . It is possible to measure particle momentum with a precision

$$\sigma(p_T)/p_T = 2 \times 10^{-5} p_T \oplus a$$

for tracks with high p_T, where $a = 1 \times 10^{-4}$ is the multiple scattering term which is small and p_T is in GeV. And the goal for the impact parameter of charged particles measurement is

$$\sigma(d_0) = \left[5 \oplus \frac{1}{p_T} \frac{10}{\sqrt{sin\theta)}} \right] \mu m$$

(p_T in GeV) important to the b-tagging. The performance of the ILD tracking system is illustrated in Figure 2.2. In the forward region, tracks are almost parallel to

the magnetic field and the resolution worsens for the measurement of the transverse momentum (p_T) and the impact parameter (d_0).

The high p_T tracks have a better resolution, see red curves.

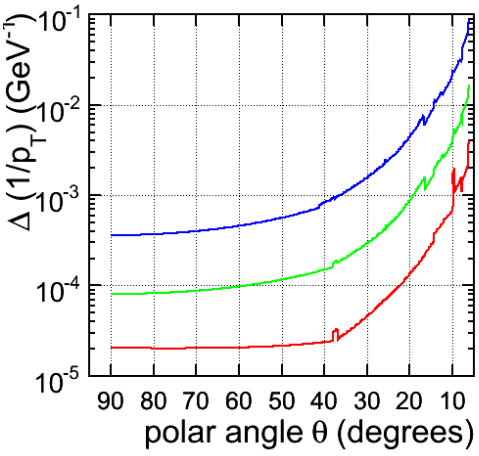

(c) Tranverse momentum resolution for different angles relative to the beam. $\frac{\sigma(p_T)}{p_T} = 2 \times 10^{-5} p_T \oplus a$

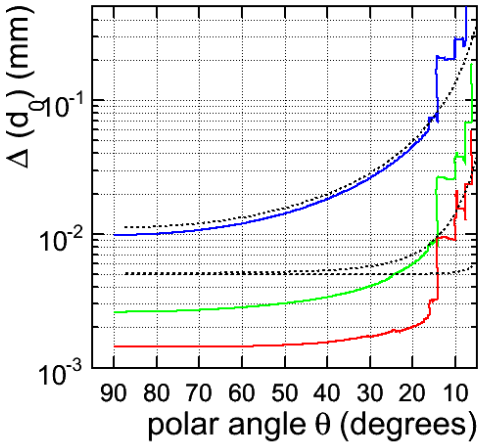

(d) The impact parameter resolution as a function of the polar angle. The dot lines show the resolutions goals parametrised as $\sigma(d_0) = [5 \oplus \frac{1}{p_T} \frac{10}{\sqrt{sin\theta)}}]\mu m$.

Figure 2.2: ILD detector performance. Colors correspond to different values of p_T: 1 GeV (blue), 10 GeV (green) and 100 GeV (red).

2.2 ILD calorimeter systems

2.2.1 Particle flow technique

As pointed out above, 70% of the decays of the W and Z bosons lead to jets in the final state. The reconstruction of invariant di-jet masses is essential to identify them. The di-jet mass resolution should thus be comparable to their natural decay widths. This requires the jet energy resolution $\Delta E_{\text{jet}}/E_{\text{jet}}$ to be about 3-4% over the entire jet energy range above 45 GeV i.e. around $30\%/\sqrt{E_{\text{jet}}}$ for jet energies below 100 GeV. This is more than a factor of two with respect to LEP which achieved a resolution of about $60\%/\sqrt{E_{\text{jet}}}$.

Traditionally, the energy of a jet is measured by the calorimeters. However this energy can be decomposed into approximately 65% of contributions from charged particles, 26% from photons and 9% from neutral hadrons. A fraction of around 1% of the energy can be carried by neutrinos present in jets from charm and bottom quarks but will not be discussed here. Moreover the tracking system which measures the momentum of charged particles is usually much more accurate than the energy measurement of the calorimeters. It is therefore more attractive to measure the majority of the energy carried by charged particles with the tracking system, while

the calorimeters measure only the energy of neutral particles as it is shown in Figure 2.3. This is the paradigm of particle flow [6].

To corroborate the previous assertion, we give an example of jet energy resolution. At the ILC, the requirement on jet energy resolution implies that the charged particles be measured in the tracker with a momentum resolution σ_{1/p_T} of about $2 \times 10^{-5}\,\mathrm{GeV}^{-1}$. The energy resolution of the calorimeters σ_E/E is expected to be better than $15\%/\sqrt{E}$ in the ECAL and better than $50\%/\sqrt{E}$ in the HCAL, with E in GeV.

Assuming these resolutions we want to show the impact on the jet energy resolution $\Delta E_{\mathrm{jet}}/E_{\mathrm{jet}}$. Following the previous prescription that charged (ch) tracks constitute 65% of the energy and are measured in the tracking system, while 26% energy contributions of photons (γ) and 9% of neutral hadrons (h^0) are measured in the ECAL and HCAL, this simple jet energy resolution reads:

$$\begin{aligned}(\Delta E_{\mathrm{jet}})^2 &= (\Delta E_{ch})^2 + (\Delta E_{\gamma})^2 + (\Delta E_{h^0})^2 \\ &\approx 4.5 \times 10^{-12} E_{jet}^4 + 30 \times 10^{-3} E_{jet}\end{aligned} \tag{2.1}$$

The numbers show that the jet energy resolution is dominated by the second term on the right-hand side coming from the calorimters up to several hundreds of GeV. Neglecting the first term coming from the tracking system, the jet energy resolution can be estimated:

$$\Delta E_{\mathrm{jet}}/E_{\mathrm{jet}} \sim \frac{30\%}{\sqrt{E\ (\mathrm{GeV})}} \tag{2.2}$$

and

$$\Delta E_{\mathrm{lepton},\gamma}/E_{\mathrm{lepton},\gamma} \sim \frac{18\%}{\sqrt{E\ (\mathrm{GeV})}} \tag{2.3}$$

The required precision is reached. With a perfect particle flow algorithm, each charged particle is reconstructed with the combination of a track and energy depositions in the calorimeters and the remaining deposits come from neutral particles. To this aim the detector must be optimized for the separation the various energy depositions in the calorimeters.

The use of a strong magnetic field and a large radius is favored to separate depositions of charged particles from neutral ones. The calorimeters must be made of dense material to reduce the lateral size of the showers thus separate them best and prevent their overlapping. This geometric separation of the showers also requires a fine granularity of the calorimeters in order for dedicated algorithms to cluster unambiguously the contributions by energy deposition of all particles. A limiting factor of the particle flow, called "confusion", is due to overlapping showers.

To conclude, particle flow technique is a very powerful tool to measure jet energies with a great resolution.

2.2.2 ECAL and HCAL calorimeters

The combined ILD electromagnetic and hadronic calorimeter systems consist of a central barrel part and two end caps. The entire barrel system is contained within the

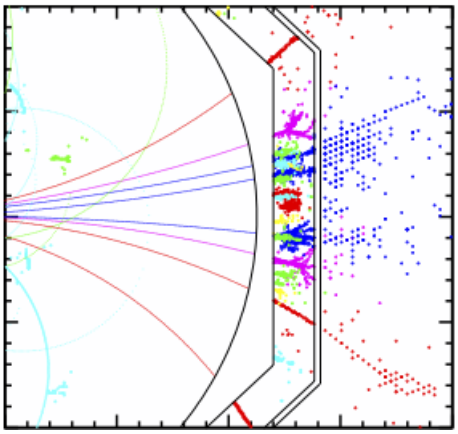

Figure 2.3: Calorimeter (Silicon-Tungsten)

volume of the cylindrical superconducting solenoid. The electromagnetic calorimeter and hadronic sections have silicon active layers between tungsten and steel absorber layers.

The main parameters, such as the aspect ratio, inner radius, depth and granularity, have been optimised using a particle flow algorithm package called Pandora.

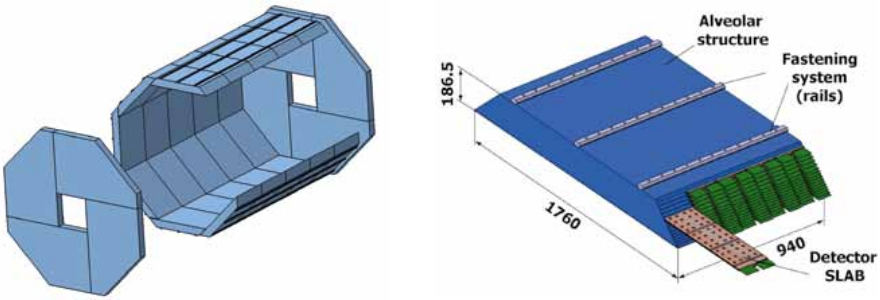

Figure 2.4: The ILD ECAL structure and details of a barrel module.

The ECAL (Figure 2.4) is segmented into 30 sampling layers corresponding to 24 X_0. The HCAL has 48 layers and a total depth of 5.5 λ, in addition to the ECAL. Several baseline technologies are considered for the instrumentation of the active layers: silicon pad diodes or scintillator strips with a transverse segmentation of 0.5 to 1 cm for the ECAL and 3×3 cm^2 scintillator tiles or gaseous devices with a segmentaion of 1×1 for the HCAL.

2.3 ILD magnet coil

The concept of a magnet coil for ILD (Figure 2.5) is a large superconducting magnet with the following parameters: desgin field of 3.5T in a 6.9 m warm bore and on a 7.35 m coil length to perform 3D magnetic calculations (including the yoke) and to study various options for the coil design.

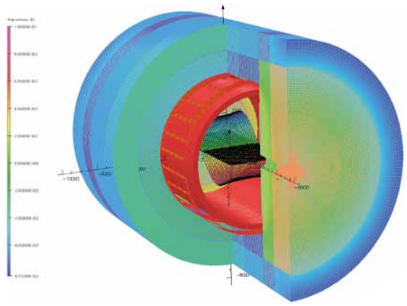

Figure 2.5: Superconducting magnet concept in ILD

2.4 B tagging

This section reviews important performances of the detector regarding top pair production at the ILC. The study of this thesis concerns mainly semileptonic top decays, where B hadrons appear. Emphasis is put here on the B tagging.

Identifying a top event relies mainly on the presence of bottom hadrons. A b-tagging is used event per event to tag jets originating from bottom hadrons. B hadrons have a larger mean life (450 ns) than other hadrons. This property allows us to identify them. The B tag value is the output of a neural network and is attached to a jet. It takes a value between 0 and 1, and is the probability of the jet to originate from a bottom hadron.

To calculate the B tag value of a jet, it is necessary to reconstruct its vertex of origin. For bottom hadrons, this will correspond to a secondary vertex with respect to the vertex of primary interaction and their decay length can be calculated (Figure 2.6).

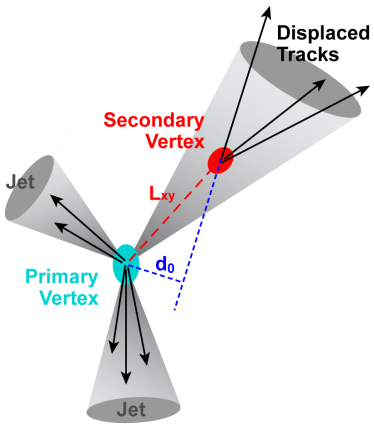

(e) Graphic of the b-tagging, using secondary vertex technique.

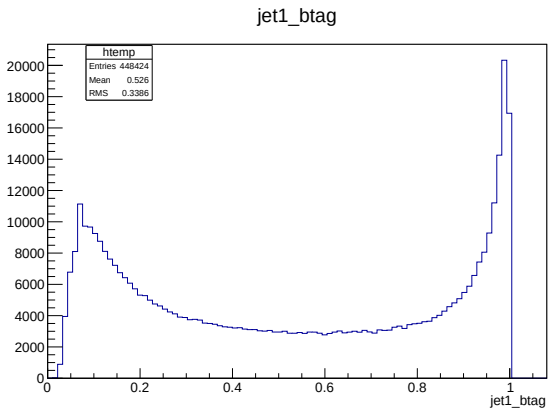

(f) Example of B tag weight distribution.

Figure 2.6: B tagging

As shown Figure 2.6 (e), the resolution of the impact parameter (d_0) measurement is essential in order to identify the secondary vertex.

B tagging at the ILC is done by the so-called LCFIVertex algorithm.

2.5 Example of LHC detector (ATLAS)

2.5.1 ATLAS performance

In order to see improvements in detector performances for ILC, in the following some parameters are compared to the ATLAS detector at the LHC [7]. Calorimeters resolutions are:

$$\sigma_E/E = \frac{10\%}{\sqrt{E}} \oplus a_{em} \text{ with } a_{em} \approx 1\% \text{ for ECAL}$$

$$\sigma_E/E = \frac{60\%}{\sqrt{E}} \oplus a_{had} \text{ with } a_{em} \approx 3\% \text{ for HCAL}$$

where ECAL is formed by liquid Argon and HCAL is a sandwich of Fe layers with scintillators tiles.

The ATLAS magnetic field is quite smaller than ILD field, $B_{ATLAS} = 2$ Tesla. It allows to measure the charge particle momentum with a precision of:

$$\sigma(p_T)/p_T = 4 \times 10^{-4} p_T \oplus a$$

where $a = \frac{1.3\times10^{-2}}{\sqrt{sin\theta}}$ is the multiple scattering term. In the case of ATLAS it is more advantatgeous to measure electron energy with the calorimeter due to its better resolution. However the material in the tracker volum degrades the momentum measurement for $p_T < 30$ GeV.

On the other hand, the precision of the impact parameter for charged particles measurement is

$$\sigma(d_0) = \left[11 \oplus \frac{1}{p_T} \frac{70}{\sqrt{sin\theta)}}\right] \mu m$$

(p_T in GeV), and again material degrades the measurement because the multiple scattering term $a = \frac{1}{p_T} \frac{70}{\sqrt{sin\theta)}}$ is too large.

2.5.2 Comparison LHC vs ILC

As shown below (Table 2.1) the performance of an ILC detector is significantly better than the performance of the ATLAS detector, greater precision in jet energy measurement, better lepton identification, higher b-tagging...

	ATLAS	ILC	use
σ_E/E *(jets)*	60 % /√E	30 % /√E	Jet energy
$\Delta p_T / p_T$ *(charged track)*	$4\cdot10^{-4}\, p_T \oplus a$	$2\cdot10^{-5}\, p_T \oplus a$	muon-momentum (*electron* at ILC)
$\sigma(d_0)$ *(impact parameter)*	$\left[11\oplus\frac{1}{p_T}\frac{70}{\sqrt{\sin\theta}}\right]\mu m$	$\left[5\oplus\frac{1}{p_T}\frac{10}{\sqrt{\sin\theta}}\right]\mu m$	b-tagging
Magnetic field	2 Tesla	3.5 Tesla	-

Table 2.1: Comparison between and LHC detector (ATLAS) and ILC detector (ILD).

Chapter 3

Reconstruction of the top quark

3.1 Top production

3.1.1 Top at a Linear Collider

In this work, top quark production will be studied assuming $\sqrt{s} = 500$ GeV and an integrated luminosity of $\mathcal{L} = 500$ fb^{-1}. Since the reaction occurs in center-of-mass, the energy and momentum conservation implies $\sum_f \vec{p}_f = 0$ and $\sum_f E_f = 500$ GeV where f are all final state particles. Top quark production has a threshold energy at $\sqrt{s} = 350GeV$ (twice the top quark mass) however at $\sqrt{s} = 500$ GeV we have slightly boosted tops ($\gamma_t = 1,43$, $\beta_t = 0,71$).

An advantatge of a LC is that beams are polarised $P(e^-) \approx \pm 80\% P(e^+) \approx \pm 30\%$ (in a realistic case). Polarisation is a very powerful tool for analysis and is determined with great precision using $e^+e^- \to W^+ W^-$.

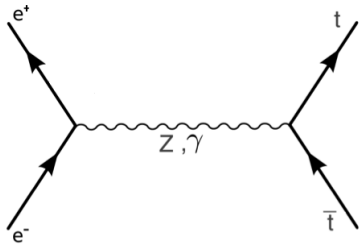

Figure 3.1: Production of $t\bar{t}$ pairs at a LC

3.1.2 Top at Hadron Collider

First, note that the $t\bar{t}$ production is completely different for the LHC and the LC. While $t\bar{t}$ is produced by strong couplings with gluons (Figure 3.2) at LHC, at LC $t\bar{t}$ interacts with Z/γ by EW couplings (Figure 3.1).

Assuming $\sqrt{s} = 7$ TeV (LHC) as the average center-of-mass energy, the effective $\sqrt{s}$ for $gg \to t\bar{t}$ is $\sqrt{s} = 580$ GeV. Not much above $e^+e^- \to t\bar{t}$ with $\sqrt{s} = 500$ GeV. In Hadron Colliders the reaction does not occur in c.o.m. so there is momentum

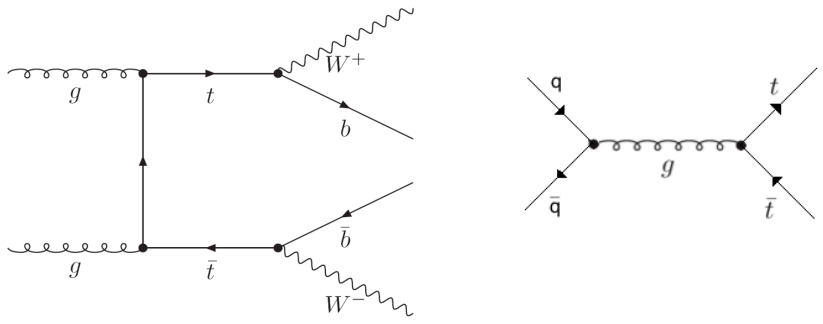

(a) $gg \to t\bar{t}$ (b) $q\bar{q} \to t\bar{t}$

Figure 3.2: Production of $t\bar{t}$ pairs at LHC. Mainly $gg \to t\bar{t}$ ($q\bar{q} \to t\bar{t}$ also happens at lower rate).

conservation only in tranverse momentum [1]:

$$\sum_f (p_x)_f = \sum_f (p_y)_f = 0 \tag{3.1}$$

As a consequence of the process $gg \to t\bar{t}$ is symmetric, the charge asymmetry measurement is diluted. One of the biggest drawbacks of LHC against Linear Colliders is that poralization is not available.

3.2 Top study at the ILC

The large mass of the top quark implies a large decay width and a short lifetime of about $0.5 \cdot 10^{-23}$ s. This suppresses hadronization before decay and therefore the spin information is preserved in its decay products. It decays dominantly via $t \to bW^+$. The pair production process $e^+e^- \to t\bar{t}$ [8] thus leads to three final states: the *fully hadronic* (46.2%) where the two W bosons decay into jets, the *semileptonic* (43.5%) where one W decays into jets and the other into a charged lepton (including τ's) and a neutrino, and the *fully leptonic* (10.3%) where both W bosons decay into leptons.

The final states in the detector are thus six jets including two b jets (jets originating from a bottom quarks) in the fully hadronic channel, four jets including two b jets, one charged lepton and missing energy in the semileptonic channel, two b jets, two charged leptons and missing energy in the fully leptonic channel. These complex final states with b-jets and leptons provides an excellent benchmark to test the detector properties as well as theoretical models.

A detailed study of top pair production at the ILC reported a signal selection efficiency of 90% with a background signal of 5% in the semileptonic decay channel and 90% signal selection efficiency with 30% background signal in the full hadronic channel. The study used a multivariate likelihood method to select signal events and

[1] The neutrino ν for $W \to l\nu$ cannot be reconstructed. The constraint $m_W^2 = (p_l + p_\nu)^2$ gives a second order equation with 2 indistinguishable solutions and is a poor method.

veto background ones. The main motivation was to measure the top mass, which was done after kinematic fitting.

The present study aims to derive the couplings $F_V^\gamma, F_A^\gamma, F_V^Z, F_A^Z$ that appear in the $t\bar{t}\gamma$ and $t\bar{t}Z$ vetices as indicated in Figure 3.3. Precision measurements at the ILC of several observables that will be described Sec. 3.3. This is not the most general model, but is a good starting point to evaluate the potential of the ILC.

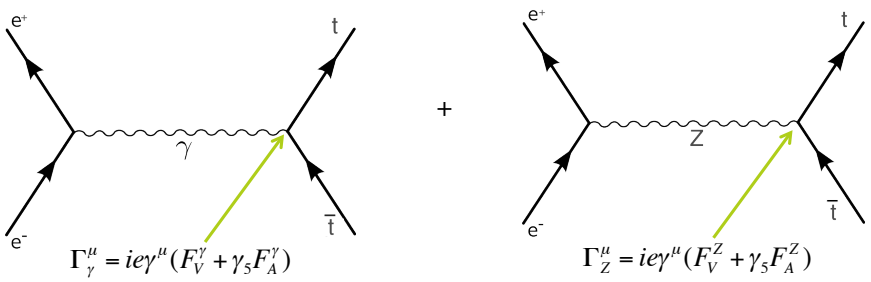

Figure 3.3: Simple model of γ,Z bosons couplings with quark top

In SM the expected values for these couplings are:

$$F_V^\gamma = -\tfrac{2}{3}$$

$$F_A^\gamma = 0$$

$$F_V^Z = +\tfrac{1}{4sin\theta_W cos\theta_W}\left(1 - \tfrac{8}{3}sin^2\theta_W\right)$$

$$F_A^Z = -\tfrac{1}{4sin\theta_W cos\theta_W}$$

There are many extensions of the SM that can affect the interaction between top quark and Z/γ bosons. For example, departure of SM values is expected if the top quark is composite.

3.3 Observables of interest

The favored observables for top pairs are the cross section, the forward-backward asymmetry A_{FB}^t and the helicity aymmetry A_{hel}^t . Since the helicity angle is defined as the angle between top quark and lepton and the forward-backward asymmetry A_{FB}^t requires the knowledge of the charge of the top quark, this study is made only for the semileptonic final state (Figure 3.4).

Cross-sections for the top study For a given polarization of the electrons (P) and the positrons (P'), the cross-section of any channel at the ILC reads:

$$\begin{aligned}\sigma_{P_-,P_+} = \; & \frac{1}{4}[(1+P_-)(1+P_+)\sigma_{RR} + (1-P_-)(1+P_+)\sigma_{LR} \\ & +(1-P_-)(1-P_+)\sigma_{LL} + (1+P_-)(1-P_+)\sigma_{RL}]\end{aligned} \tag{3.2}$$

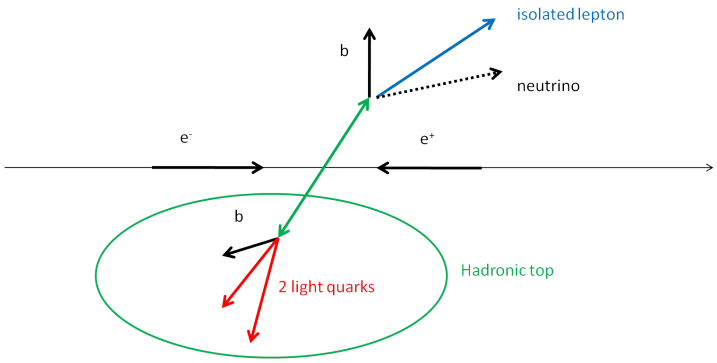

Figure 3.4: Picture of the semileptonic top decay. The strategy proposed is to reconstruct the hadronically decaying top quark and use the lepton to know its charge.

with the notations R/L for +/- 100% longitudinally polarised electrons or positrons. A null polarisation thus stands for unpolarised beams.

In the limit $m_e/E \to 0$, valid here since $E = 250\,\text{GeV}$ approximately, $\sigma_{LL} = \sigma_{RR} = 0$ at tree level: $e^-_L e^+_L$ and $e^-_R e^+_R$ do not couple to photons and Z bosons due to helicity conservation. The cross-section reduces to:

$$\sigma_{P_-,P_+} = \frac{1}{4}\left[(1 - P_- P_+)(\sigma_{LR} + \sigma_{RL}) + (P_- - P_+)(\sigma_{RL} - \sigma_{LR})\right] \tag{3.3}$$

Two polarization states are needed to measure the cross-sections $\sigma_{L,R}$ and $\sigma_{R,L}$. The two configurations could equally share the luminosity while leading to larger statistics as far as statistical errors are concerned. The one with a predominantly left-handed electron and a right-handed positron $(-|P_-|, |P_+|)$ and the opposite $(|P_-|, -|P_+|)$ are preferred.

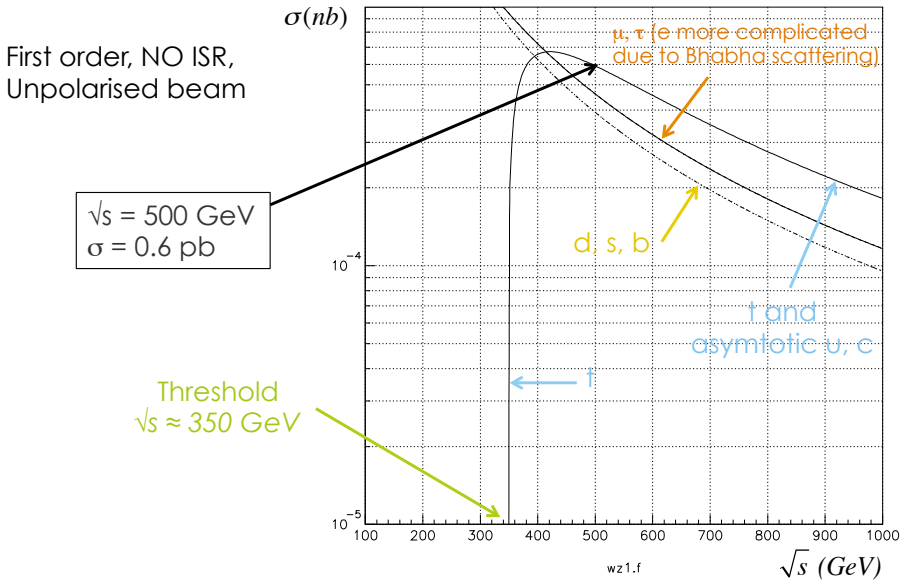

Figure 3.5: Cross section for $e^+e^- \to t\,\bar{t}$ as function of $\sqrt{s}$ for unpolarised beams.[9]

Forward-backward asymmetry A^t_{FB} The forward-backward asymmetry for the process $e^+e^- \to t\bar{t}$, A^t_{FB}, is defined by:

$$A^t_{FB} = \frac{\sigma(\cos\theta_t > 0) - \sigma(\cos\theta_t < 0)}{\sigma(\cos\theta_t > 0) + \sigma(\cos\theta_t < 0)} \tag{3.4}$$

with θ_t the top polar angle with respect to the initial direction of the electron and

$$\sigma(\cos\theta_t) = \int \frac{d\sigma(e^-e^+ \to t\bar{t})}{d\cos\theta_t}\, d\cos\theta_t$$

where the sum has been made over the two configurations of polarization.

This requires that the charge of the top quark is known. In this process involving only two particles in the center-of-mass frame, a forward anti-top $\bar{t}$ (with $\cos\theta_{\bar{t}} > 0$) will contribute to the backward part ($\cos\theta_t < 0$). In this study, this charge is deduced from that of the lepton of the semileptonic decay of the top pair.

If an equal luminosity is spent in the configurations $(|P_-|, -|P_+|)$ and $(-|P_-|, |P_+|)$, the forward-backward asymmetry is independent of the polarization, only the number of measured events will differ for A^t_{LR}. This asymmetry was already estimated using the full hadronic decay channel, where the charge of the top was given by the b jet. The result is $A^t_{FB} = 0.334 \pm 0.0079$, that is, a 2% relative uncertainty. However, the efficiency of charge identification of a b jet is 28% with a 75% purity, while the misidentification of the charge of a lepton is less than 0.1% with an efficiency better than 85% as will be shown in this study.

Another possibility is to use polarized forward-backward asymmetries, i.e. forward-backward asymmetries measured in both configurations of polarization: $A^t_{FB(e_R)}$ when the electron beam is mostly right-handed ($P > 0$) and $A^t_{FB(e_L)}$ when it is mostly left-handed. 2% relative uncertainties were found for both polarised asymmetries using the charge identification of the b jet. Using the semileptonic final state to deduce the charge of the top quark is an advantage compared to these methods, and can lead to a relative precision of 0.5%.

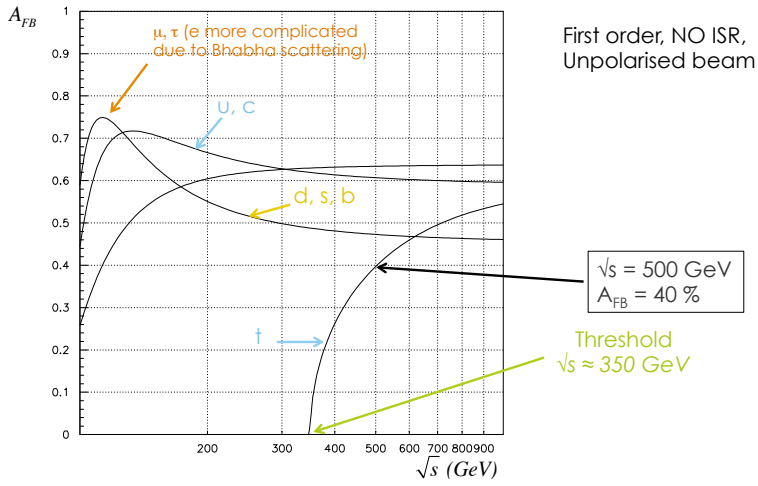

Figure 3.6: Forward-backward asymmetry for $e^+e^- \to t\,\bar{t}$ as function of $\sqrt{s}$ for unpolarised beams.[9]

Helicity asymmetry The helicity asymmetry for the process $e^+e^- \to t\bar{t}$, A^t_{hel}, is defined by:

$$A^t_{hel} = \frac{\sigma(\cos\theta_{hel} > 0) - \sigma(\cos\theta_{hel} < 0)}{\sigma(\cos\theta_{hel} > 0) + \sigma(\cos\theta_{hel} < 0)} \tag{3.5}$$

with θ_{hel} the helicity angle defined as the angle between the direction of the lepton in the top rest frame and the initial direction of the top quark in *lab* frame.

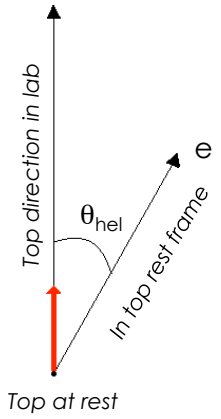

(c)

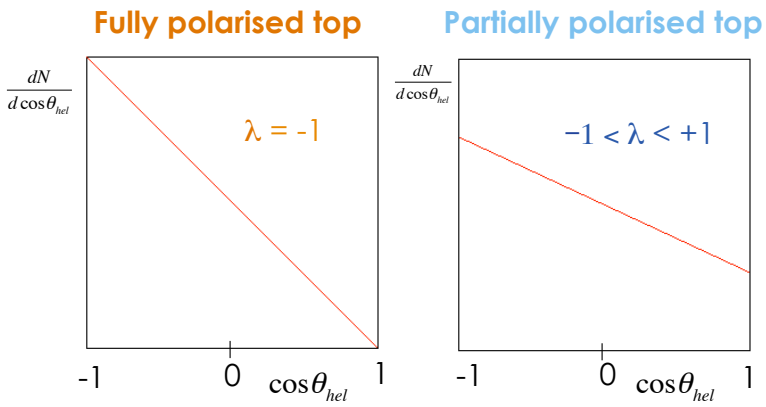

(d) Helicity distributions.

Figure 3.7: Helicity distribution is defined as an straight line given by: $\frac{dN}{dcos\theta_{hel}} = N_0(1 + \lambda cos\theta_{hel})$ where λ is the top polarisation.

In Figure 3.7, the parameter λ is the slope of this straight line and is related to helicity asymmetry by the relation: $\lambda = 2A_{hel}$

Theoretical considerations In order to understand better the couplings between fermions and bosons, let us consider a theoretical analysis of the process in Figure 3.8.

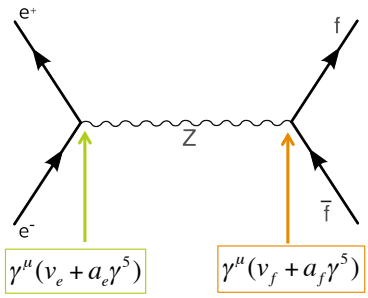

Figure 3.8: $e^+e^- \to f\bar{f}$ at Born level without Initial State Radiation and unpolarised cross sections, where f = any fermion

.

$$\frac{d\sigma}{dy} = \frac{3}{8}\sigma_{pt}N_c^f\beta_f\left[g_1(1+y^2) + 4\mu_f g_2(1-y^2) + 2y\beta_f g_3\right] \tag{3.6}$$

In Eq.3.6, $y = cos\theta$ where θ is scattering angle, $\sigma_{pt} = \frac{4\pi}{3}\frac{\alpha^2}{s}$ is the QED pointlike cross section, $\beta_f = \sqrt{1-4\mu_f}$ ($\mu_f = m_f^2/s$) is the fermion velocity and $N_c^f = 1$ (f=leptons) and $N_c^f = 3$ (f=quarks) is the number of colour state.

$$\begin{aligned} g_1 &= Q_f - 8\nu_e\nu_f Q_f Re(\chi_0) + (\nu_e^2 + a_e^2)(\nu_f^2 + a_f^2 - 4\mu_f a_f^2)16\,|\chi_0|^2 \\ g_2 &= Q_f - 8\nu_e\nu_f Q_f Re(\chi_0) + (\nu_e^2 + a_e^2)\nu_f^2 16\,|\chi_0|^2 \\ g_3 &= -8a_e a_f Q_f Re(\chi_0) + (2\nu_e a_e)(2\nu_f a_f)16\,|\chi_0|^2 \end{aligned} \tag{3.7}$$

where Q_f is fermion charge ($Q_f = +2/3$ for top quark) and

$$\chi_0 = \frac{G_F M_Z^2}{8\pi\alpha\sqrt{2}} \frac{s}{s - M_Z^2 + i\Gamma_Z M_Z}$$

Note that:

$$\frac{G_F M_Z^2}{8\pi\alpha\sqrt{2}} = \frac{1}{16 s_W^2 c_W^2}$$

where $s_W = sin\theta_W$.

Therefore to obtain theoretical expressions of A_{FB} and σ we must integrate Equation 3.6 over y in $[-1, +1]$. Results are shown below.

Cross section (g_3 term vanishes)

$$\sigma = \sigma_{pt} N_c^f \beta_f \left[g_1 + 2\mu_f g_2\right]$$

so $\sigma \to 0$ if $\beta_f \to 0$ which is a well known result. Note also that in pure QED (Z supressed), $g_1 = g_2 = Q_f^2$ therefore:

$$\sigma = \sigma_{pt} N_c^f Q_f^2 \beta_f [1 + 2\mu_f] = \sigma_{pt} N_c^f Q_f^2 \frac{\beta_f}{2} \left[3 - 2\beta_f^2\right]$$

also well known result. And if $\beta_f \to 1$ $\sigma = \sigma_{pt} N_c^f Q_f^2$ as expected.

Forward-Backward asymmetry (g_3 survives)

$$A_{FB} = \frac{3}{4}\beta_f \frac{g_3}{g_1 + 2\mu_f g_2}$$

so $A_{FB} \to 0$ if $\beta_f \to 0$ which is not so well known. If $\beta_F \to 1$ $A_{FB} = \frac{3}{4}\frac{g_3}{g_1}$ ($\mu_f \to 0$). This is a relatively simple result.

The dependence on the center of mass energy of the total cross-section and the Forward Backward asymmetry are presented in Figures 3.5 and 3.6.

Including higher order EW corrections The authors of [9] have calculated elctroweak corrections. In Figure 3.9 A_{FB} and σ are shown as a function of energy in c.o.m. EW corrections at $\sqrt{s} = 500$ GeV are small. It is possible to work at Born level with small theoretical errors.

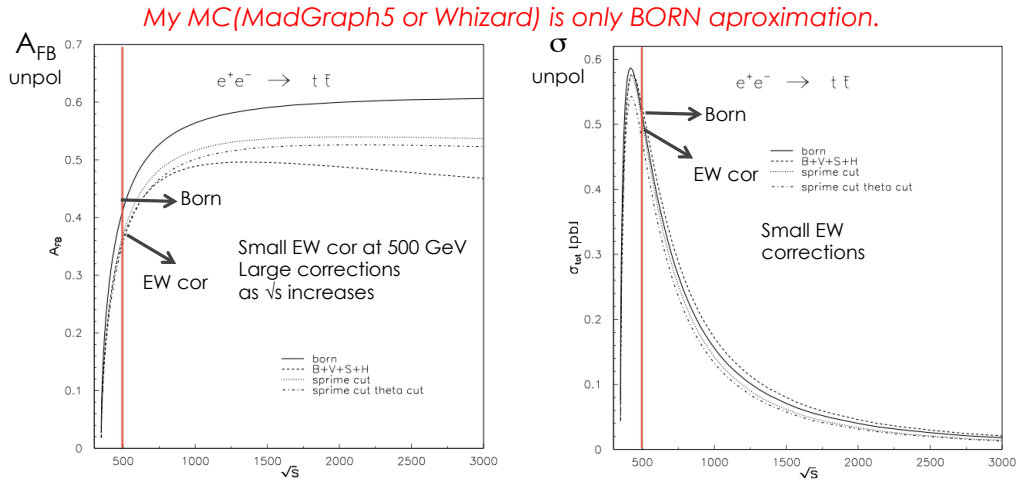

Figure 3.9: Higher order Electroweak corrections for A_{FB} and σ [10]

Initial State Radiation (ISR) In a realistic case there usually is radiation coming from beams, i.e. an electron radiates a photon which is known as Initial State Radiation. As shown in Figure 3.10, the effect of ISR in analysis is small. Due to $\sum_f \vec{p}_f \neq 0$ there is a tail in reconstruction of neutrino variables and other distributions where it is assumed that the total energy of each top is $E_{top} = 250$ GeV (boosts to top rest frame, etc...).

In this analysis we will consider an effective energy in the center of mass of $\sqrt{s}_{eff} = 482$ GeV as the energy carried away by ISR is typically ~ 18 GeV.

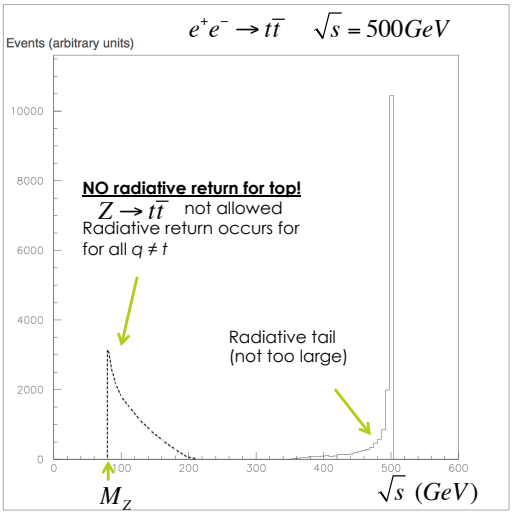

(e) Invariant mass of $t\bar{t}$

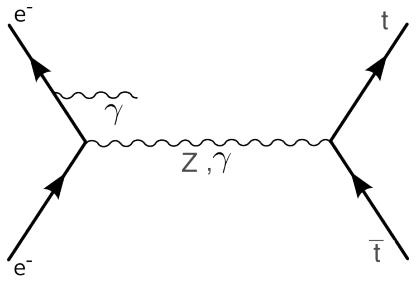

(f) Feynman diagram including ISR

Figure 3.10: Initial State Radiation

3.4 Considerations for the backgrounds

The highest cross-sections of the physical processes at the ILC were given Sec. 3.3. In view of these figures and the topology of the semileptonic decay mode studied, preliminary considerations for the backgrounds can lead the next steps of the analysis.

Other top final states One of the main background to this top pair production analysis is the top itself in other decay modes. In particular if because of misidentification or contaminations in the lepton selection, some leptons are found and kept in the full hadronic final state.

This could be the case since typically around 10% of bottom mesons decay into a charged lepton plus additional particles. However they should be embedded in a jet rather than isolated like the lepton of the top decay.

Fully hadronic top decay modes constitute 46.2% of all top pair decay modes and it is thus of the same order than the semileptonic mode. Due to its very similar final state at the parton level, a non negligible fraction of this channel may enter the selections and bias the observables considered in this study.

The full leptonic decay channel of the top pairs is another major background for semileptonic studies. Indeed, one lepton can be found and enter the selections for the semileptonic top. Too much missing energy may be involved and it could be a way to reject these events, as well as finding incoherent W and top masses.

A problem will arise if the second lepton is a τ decaying hadronically, forming a jet structure. However it should be discriminated from a real jet for it contains fewer tracks.

W pairs The W pair background is 10 times larger than the top pair production. It is very forward peaked since it involves mainly a neutrino exchange in the t-channel. This process is to be checked carefully and strongly suppressed, since any contamination at the 1% level leads to 10% impurities in the top events selected.

Only its semileptonic final state contains a lepton from a W boson but this must be strongly reduced by the identification of b jets .

Negligible backgrounds The processes involving a t-channel diagram are the largest cross-sections. In particular, the Bhabha scattering ($e^+e^- \to e^+e^-$) is two orders of magnitude above the top pair production. However, the topology of such events is rather simple and leads either to very forward electrons which may not be measured, or two energetic and well identified electrons.

The sum of all di-lepton channels is larger than the top pair production cross-section. However, the topology is again clearer: due to these highly energetic leptons, the events will appear as back-to-back di-jets. In the case of a gluon emission for quarks, the jets are still expected not to contain a lepton faking that of a W.

The cross-sections of Zγ and $\gamma\gamma$ channels are both up to 5 times larger than that of the top pair but should again lead to simpler topologies.

The ZZ background is comparable in cross-section with top pair events, but the major decay channel that can fake the top pair topology is: $e^+e^- \to ZZ \to b\bar{b}\tau^+\tau^-$,

with one tau lepton decaying into jets and the other into leptons. The branching ratio of these processes is $\approx 0.2\%$, which appears to be negligible at this level.

3.5 Extraction of physics

As it was mentioned before, polarisation is a very powerful tool for analysis. At LC electron and positron beams can be polarised so it is very useful to collide e^+e^- with the two following polarisations[2]:

$$\begin{array}{l} P(e^-) = +80\%/P(e^+) = -30\% \\ P(e^-) = -80\%/P(e^+) = +30\% \end{array} \tag{3.8}$$

Therefore there are 6 observables in total (see section 3.3), cross section, forward-backward asymmetry and helicity asymmetry for each polarisation:

$$\begin{array}{l} \sigma(+)\ A_{FB}(+)\ \lambda_{hel}(+)\ (+ = e_R^-) \\ \sigma(-)\ A_{FB}(-)\ \lambda_{hel}(-)\ (+ = e_L^-) \end{array} \tag{3.9}$$

In practice systematic errors cancel out in A_{FB} and λ_{hel}, therefore with $A_{FB}(\pm)$, $\lambda_{hel}(\pm)$ (4 observables) there is enough information to calculate the four couplings $F_V^\gamma, F_A^\gamma, F_V^Z, F_A^Z$. In the next section, the most important experimental aspects of these measurements are discussed.

3.6 MC simulation

As it has mentioned before, this study is based only in the semileptonic channel of the process $e^+e^- \to t\bar{t}$. The events have been built by using a full simulation for ILD detector (*Mokka + Whizard software*) [11]. The data has been provided by researchers from the institute LAL in Orsay (Paris).

The polarisation of the simulated events is not realistic due to the beams are fully polarised:

$$P(e^-) = +100\%\ P(e^+) = -100\%\ \textit{for}\ e_R^- e_L^+$$
$$P(e^-) = -100\%\ P(e^+) = +100\%\ \textit{for}\ e_L^- e_R^+$$

However if we make a rescaling of the obtained results from the data, we can obtain realistic results $P(e^-) = \pm 80\%, P(e^+) = \pm 30\%$ (See section 3.10). The following table shows the number of events (N) there are for each polarization.

	$e_L^- e_R^+$	$e_R^- e_L^+$
N	448424	179914

Table 3.1: Number of events.

In the data we can find the generated MC particles and the particles detected[3] by the ILD dectector.

[2] $\pm 80\%$ for e^- and $\pm 30\%$ for e^+ are realistic values, nowadays is not posible to get fully polarised electrons and much less positrons

[3] It really is a quite realistic simulation of what the ILD detector will be able to measure.

3.7 Top reconstruction

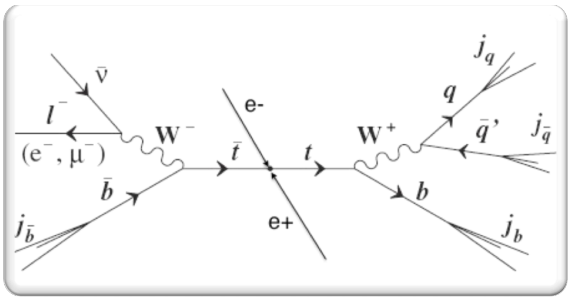

Figure 3.11: Semileptonic top events.

The most interesting channel in top pair production is the semileptonic top events (Figure 3.11, i.e. one top goes to $t \to l\nu b$ (leptonic side) and the other one $t \to j_1 j_2 b$ (hadronic side). These events originate in the W decays $W \to e\nu, \mu\nu, \tau\nu(3)$ and $W \to ud, cs(6)$ with $BR(W \to e\nu) = 1/9$ which leads to $BR\,[t\bar{t} \to (e,\mu)(jets)] = 2 \cdot 2/9 \cdot 6/9 = 30\%$. If τ's are included taking into account that $BR(\tau \to e, \mu) = 34\%$ then $BR\,[t\bar{t} \to (e,\mu)(jets)] = 35\%$. But leptons from τ's have different spectrum (soft leptons) and $t \to l + 3\nu + b$. Anyway leptonic τ's increase total sample by less tant 6%.

To succeed in the reconstruction of semileptonic channel, some detector properties are required such that all detector capabilities are at its best. The detector must be able to identify leptons (e,μ), neutrino reconstruction requires a good hermiticity, good b-tagging and precise measurements of lepton momentum and jet energy.

3.8 Reconstruction problems in semileptonic events

For hadronic top reconstruction there are two possibilities:

$$\begin{aligned} P_{top}(1) &= P(b_1) + P(j_1) + P(j_2) \\ P_{top}(2) &= P(b_2) + P(j_1) + P(j_2) \end{aligned} \tag{3.10}$$

Where (b_1, b_2) are the two b-jets and (j_1, j_2) are the other two jets of the event. When a b-jet is assigned to the top, sometimes the wrong b-jet is chosen therefore the reconstructed top leads to poor results.

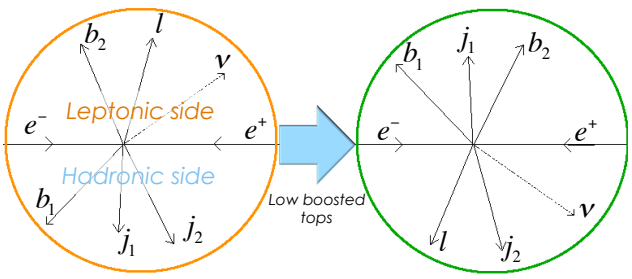

Figure 3.12: Left: Ideal $e^+e^- \to t\,\bar{t}$ event. Right: Real events where b-jets are mixed up

This problem disappears if both top quarks are boosted [12].

3.8.1 Result for top invariant mass

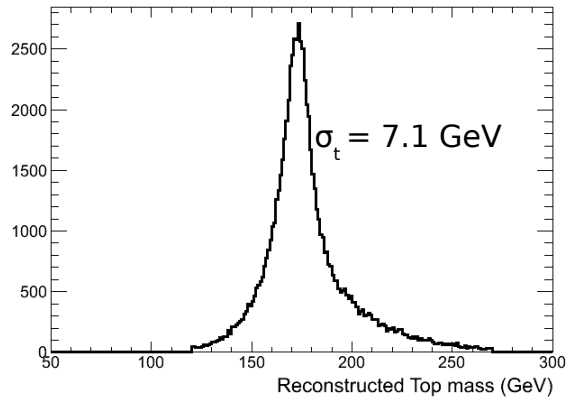

Figure 3.13: Distribution of reconstructed top mass in hadronic side $t \to bj_1j_2$

Data to analyse top quark properties are taken from a full simulation for ILD detector GEANT4 (*Mokka Software*) with an efficiency $\varepsilon_{cuts} \approx 70\%$ for semileptonic events and a background $\sim 5\%$ (WW events and $t \to b \to l$ events). The reconstructed mass distribution has a width of 7.1 GeV. The collected data allows to extract the peak position to 25 MeV (statistical error). For a discussion of top measurements at the ILC. See for instance [13].

It possible to obtain a more accurate result with improved P-flow techniques (see 2.2.1), the top mass width (σ_{top}) can reach a value of ~ 5 GeV, which gives access to $\Gamma_{top} \sim 1.5$ GeV. An interesting point to comment is that measurement of Γ_{top} implies measurement of $|V_{tb}|$ as shown following equation,
$\Gamma_{top} = \frac{G_F M_{top}^2}{8\pi\sqrt{2}}|V_{tb}|^2(1-\mu)^2(1-2\mu)$ + QCD corrections, where $\mu = \frac{M_W^2}{M_{top}^2}$. This parameter has been mesured at LHC in the single top production.

3.8.2 Migration effect

The measurement of A_{FB} is degraded due to migration effect. The A_{FB} for $\sigma(-)$ is 25 % for reconstructed events, away from the MC result 40 % (Figure 3.14). The reason is that b_1 and b_2 have been mixep up. It produces a small effect for M_{top} but has a large impact in A_{FB}(-). Error happens in about 30% of events where the maximum is 50%.

On the other hand, for $\sigma(+)$ there is no problem. To find an explanation to this result, one has to perform an helicity analysis (Figure 3.15) which shows that:

$$\begin{array}{l} P(\mathrm{e}^-) = +1\text{: } \vec{p}_b \text{ of b-quark goes in the direction of } \vec{p}_t \\ P(\mathrm{e}^-) = \text{-}1\text{: } \vec{p}_b \text{ of b-quark goes in the direction oposite to } \vec{p}_t \end{array} \tag{3.11}$$

This helicity analysis is valid only in the 30% of the cases where W boson have a left handed helicity. Usually W has no helicity (70%).

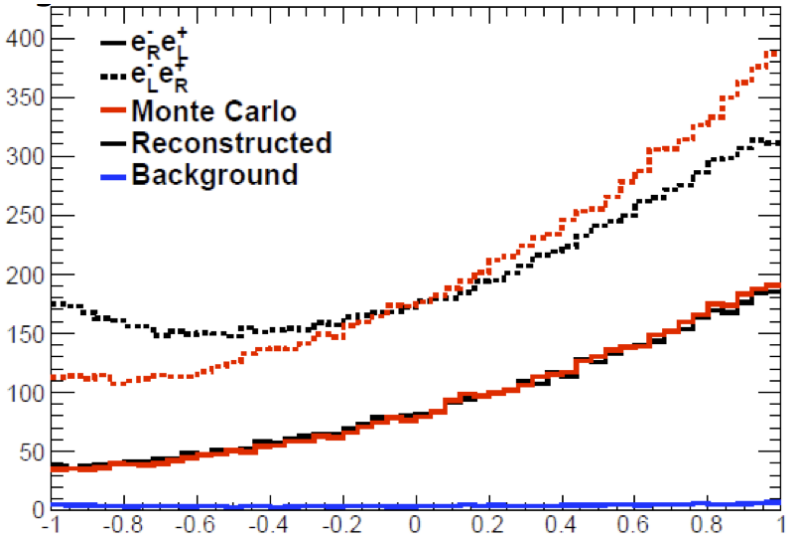

Figure 3.14: Angular distribution of top quark for both polarisations $e^-_L e^+_R$ (small σ) and $e^-_R e^+_L$ (large σ).

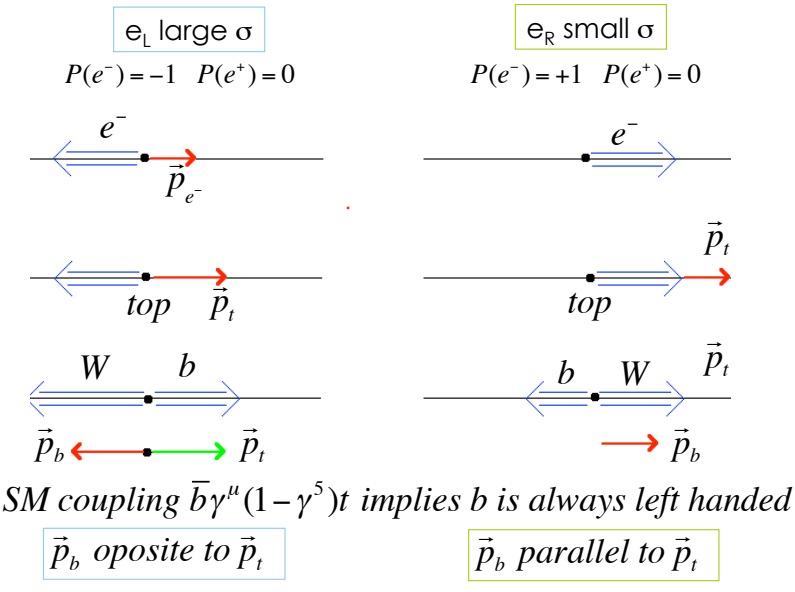

Figure 3.15: Helicity analysis of top quark production and its decay for $e^-_L e^+_R$ (left side) and $e^-_R e^+_L$ (right side).

In order to throw away wrong the reconstructed events (wrong b-jet) it is desirable to use all posible observables in the event. For example, to analyse the leptonic side the best obervables are shown in Table. 3.2.

Observable	**Calculations**	**Input value**
$M_t^2 = (p_b + p_l + p_\nu)^2$	$\vec{p}_\nu = -\sum_f \vec{p}_f$	$M_t = 173$ GeV
$E_t = E_b + E_l + E_\nu$	$E_\nu = 500$ GeV $- \sum_f E_f$	$E_t = 250$ GeV
$E_b^* = E_b$ in top rest frame	$E_b^* = \frac{1}{2}\frac{M_t^2 - M_W^2 - M_b^2}{M_t}$	$E_b^* = 68$ GeV
$cos\theta_{bW}$ = angle between b and W_{reco}	$\vec{p}_W = \vec{p}_l + \vec{p}_\nu$	$\langle \cos\theta_{bW} = 0.26 \rangle$

Table 3.2: Observables of the strategy, the calculation of some variables and their input values.

Thereafter the input values and observable distributions are used to build a χ^2 in the following way:

$$\chi^2 = \left(\frac{M_t - 173}{\sigma_{M_{top}}}\right)^2 + \left(\frac{E_t - 250}{\sigma_{E_{top}}}\right)^2 + \left(\frac{E_b^* - 68}{\sigma_{E_b^*}}\right)^2 + \left(\frac{cos\theta_{bW} - 0.26}{\sigma_{cos\theta_{bW}}}\right)^2 \quad (3.12)$$

Migration effect must be reduced by taking the b-quark with smallest χ^2.

3.9 Analysis of the leptonic side

3.9.1 Distributions of main observables

In Figure 3.16 we show the distributions of the four observables mentioned before for $e_L^- e_R^+$ polarisation.

The blue curve shows events in which we succeed to get the correct choice of the b-quark, the green curve shows the case when the wrong b-quark is chosen and finally the dotted line gives the total number of reconstructed events.

These distributions have been obtained with ROOT (A Data Analysis Framework developed at CERN).

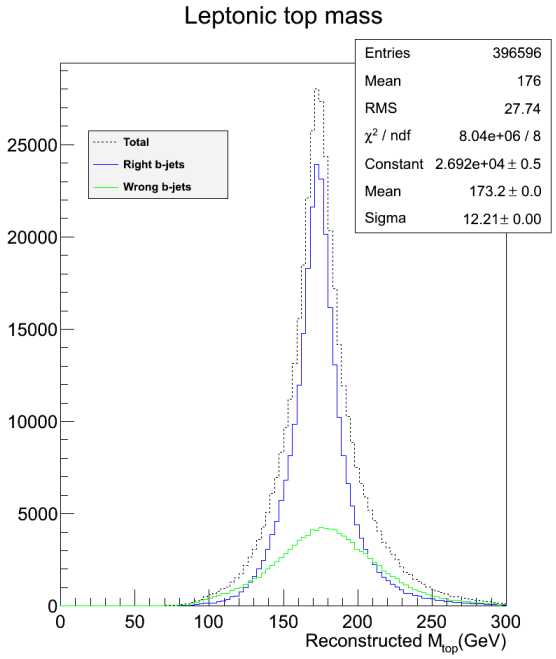

(g) Reconstructed top mass.

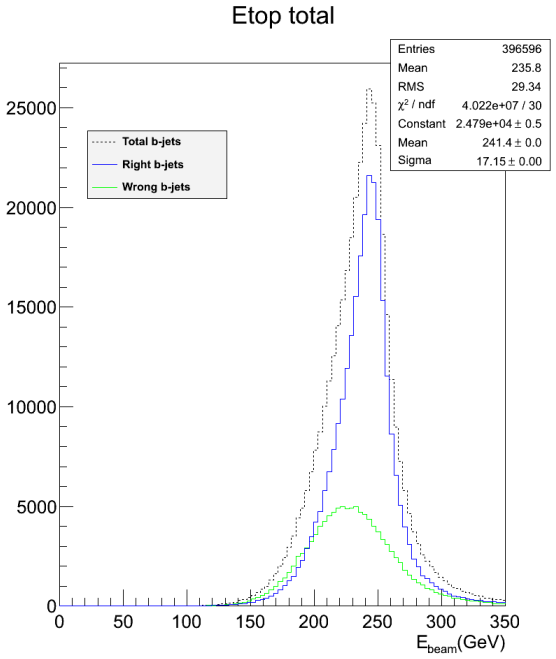

(h) Total energy of top.

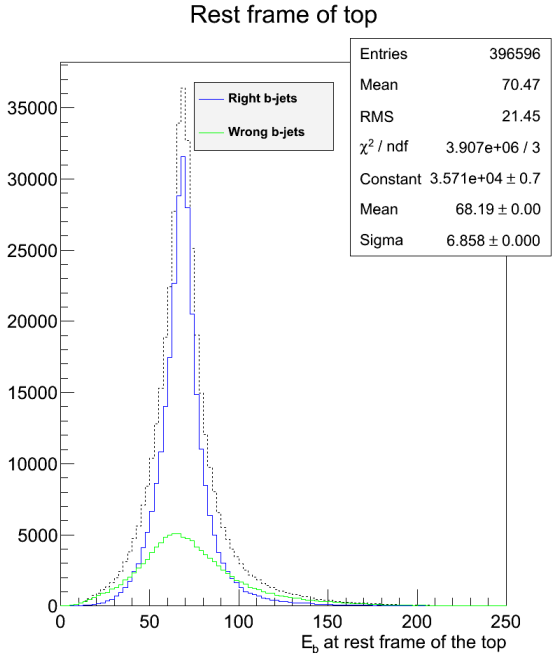

(i) Energy of b-jet at top rest frame.

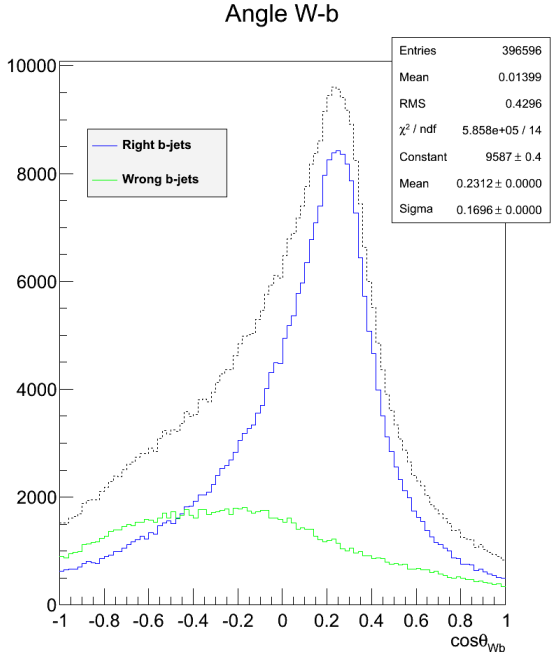

(j) Angle between b-jet and W.

Figure 3.16: Distributions of the four observables for $e_L^- e_R^+$ polarisation.

Following in Figure 3.17 shown as before the four observables distributions but now for $e_R^- e_L^+$ polarisation.

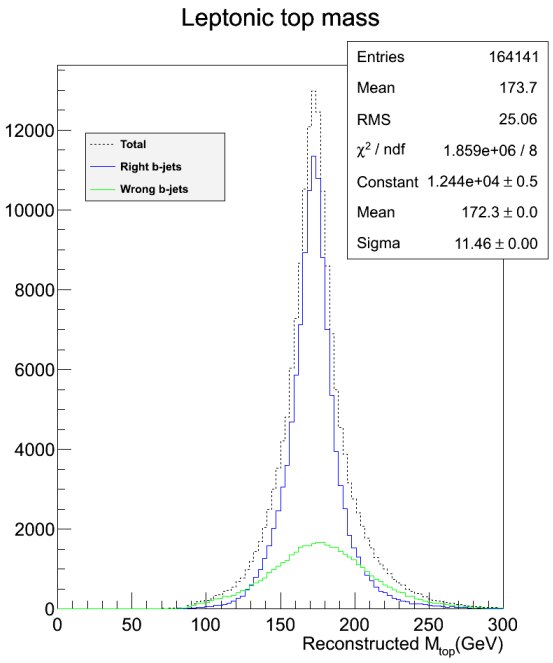

(k) Reconstructed top mass.

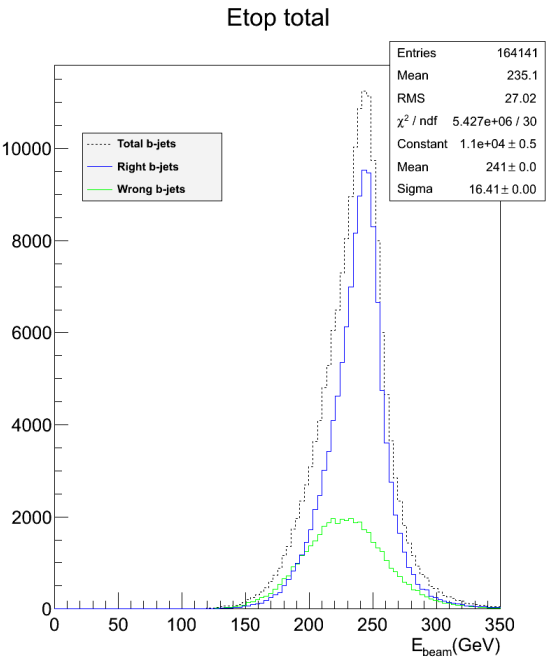

(l) Total energy of top.

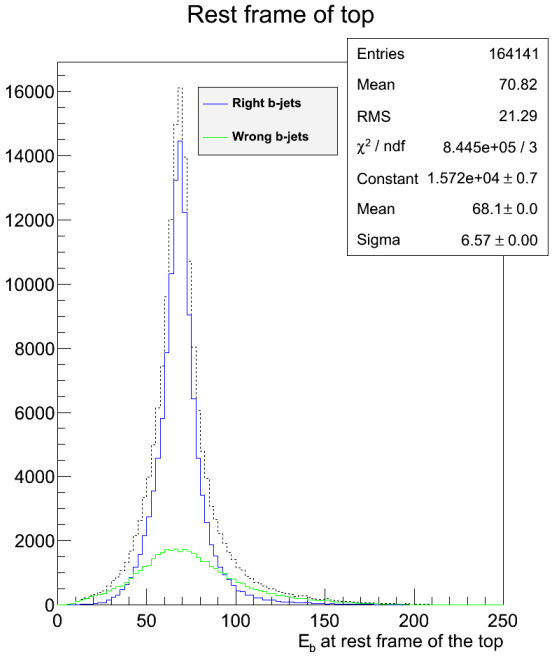

(m) Energy of b-jet at top rest frame.

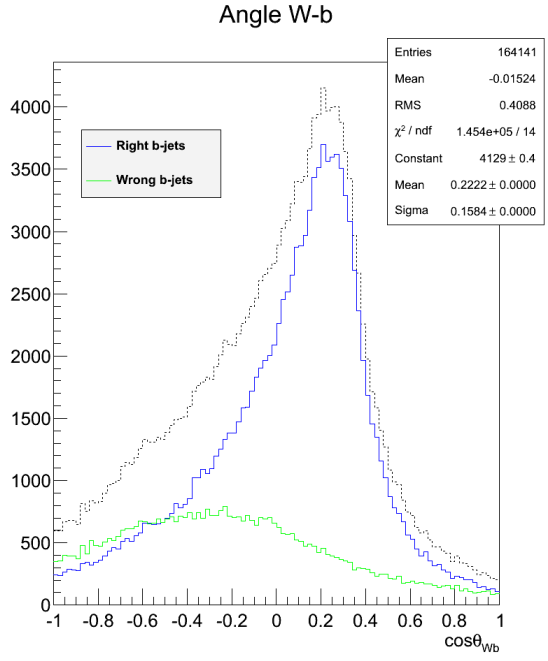

(n) Angle between b-jet and W.

Figure 3.17: Distributions of the four observables for $e_R^- e_L^+$ polarisation.

3.9.2 χ^2 analysis

Once the strategy has been presented, we can analyse the results of the χ^2 analysis in Table 3.3. The aim of this analysis is to keep small the number of wrong-reconstructed events (b-quarks mixed up) but still maintain good efficiency.

(e^-_R, e^+_L)	Small σ	
	Efficiency (%)	Wrong-reco(%)
χ^2 without cuts	91,2	27,3
$\chi^2 < 250$	81,6	23,1
$\chi^2 < 200$	77,4	21,4
$\chi^2 < 150$	71,2	18,9
$\chi^2 < 100$	61,5	15,4
$\chi^2 < 50$	45	10,4

(e^-_L, e^+_R)	Large σ	
	Efficiency (%)	Wrong-reco(%)
χ^2 without cuts	88,4	29,8
$\chi^2 < 250$	76,8	25,4
$\chi^2 < 200$	72,3	23,5
$\chi^2 < 150$	65,5	20,7
$\chi^2 < 100$	55,7	16,8
$\chi^2 < 50$	40	11,2

Table 3.3: Tables above show how efficiency and wrong-reco events vary when χ^2 cuts are applied. *Efficiency: number of reconstructed events from total. Wrong-reco: the percent of wrong reconstructed events.*

If efficiency is reduced to about 50% only a 10% of the reconstructed events are wrong b's. The following Figures 3.18 and 3.19 show how migration effect dissapears almost totally when $\chi^2 < 50$ for both polarisations.

(e^-_L, e^+_R)	Large σ					
	Efficiency (%)	Wrong-reco(%)	A_{FB} truth	A_{FB} reco	$\lambda_{hel,lepton}$ truth	$\lambda_{hel,lepton}$ reco
χ^2	88,4	29,8	33	18,6	-0,45	-0,49
$\chi^2 < 50$	40	11,2	33	30,3	-0,45	-0,62

Table 3.4: A_{FB} and λ_{hel} (slope) values before cutting in χ^2 and for $\chi^2 < 50$. $e^-_L e^+_R$ polarisation.

(e^-_R, e^+_L)	Small σ					
	Efficiency (%)	Wrong-reco(%)	A_{FB} truth	A_{FB} reco	$\lambda_{hel,lepton}$ truth	$\lambda_{hel,lepton}$ reco
χ^2	91,2	27,3	46	42,5	0,58	0,53
$\chi^2 < 50$	45	10,4	46	45,8	0,58	0,59

Table 3.5: A_{FB} and λ_{hel} (slope) values before cutting in χ^2 and for $\chi^2 < 50$. $e^-_R e^+_L$ polarisation

As we predicted before the A_{FB} needs the $\chi^2 < 50$ cut to obtain a good result. On the other hand we can keep $\chi^2 < \infty$ for the λ_{hel} due to it does not suffer the migration effect.

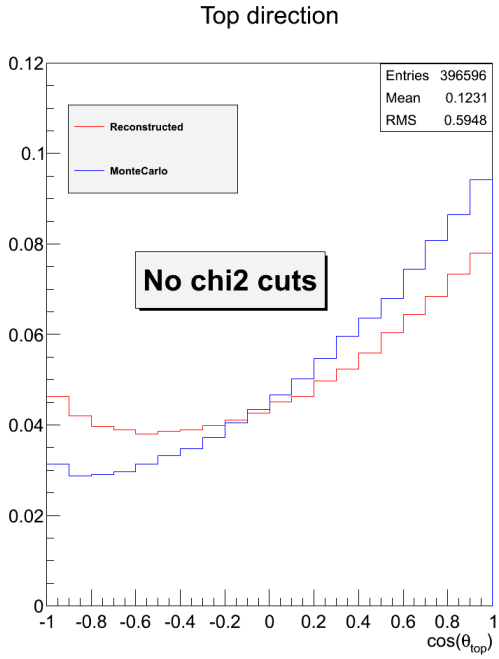

(o) Top angular distribution (no χ^2 cuts)

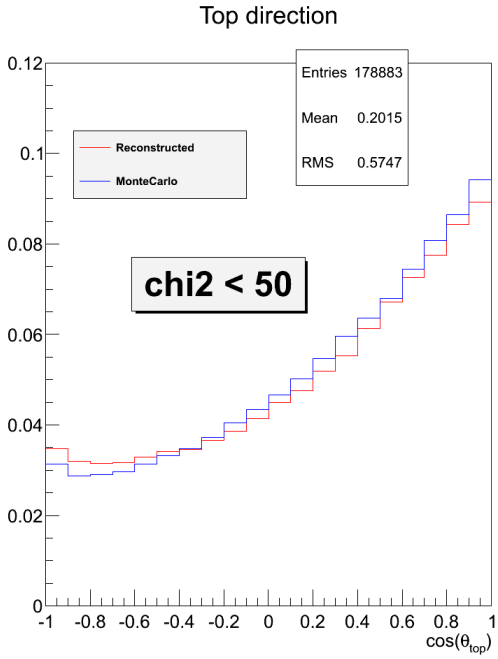

(p) Top angular distribution ($\chi^2 < 50$)

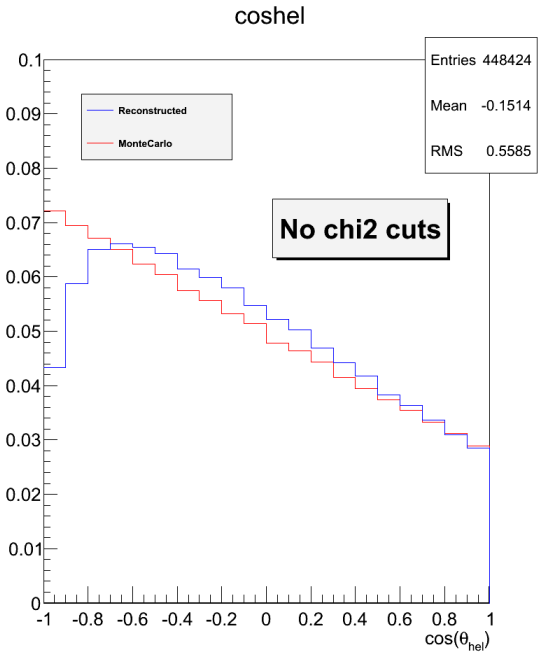

(q) Helicity distribution (no χ^2 cuts)

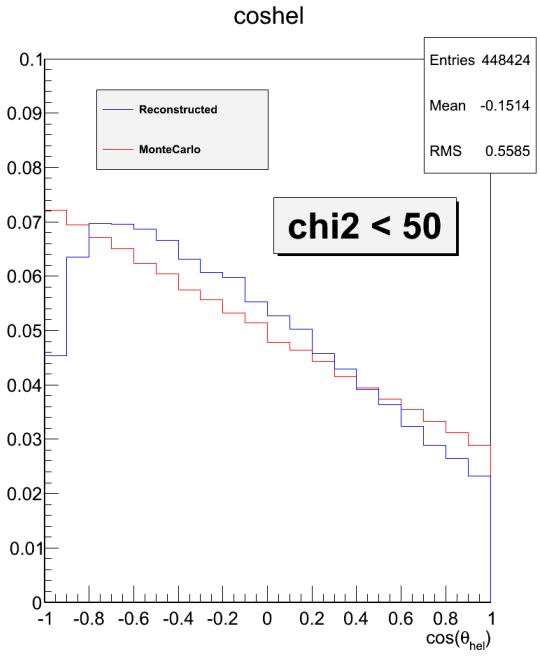

(r) Helicity distribution ($\chi^2 < 50$)

Figure 3.18: χ^2 analysis for A_{FB} and helicity angle ($e_L^- e_R^+$)

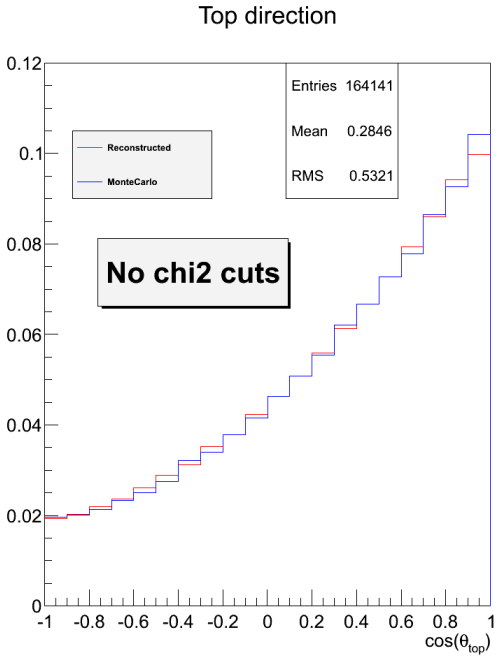

(s) Top angular distribution (no χ^2 cuts)

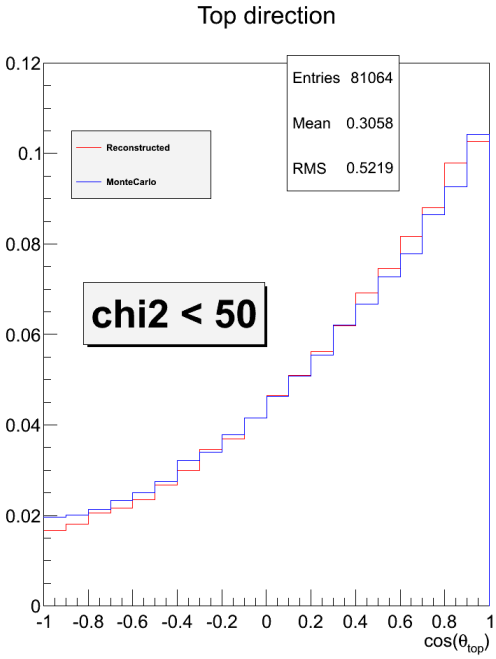

(t) Top angular distribution ($\chi^2 < 50$)

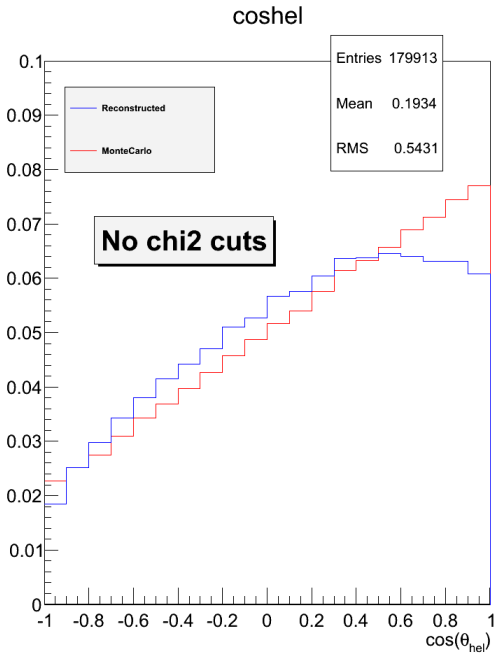

(u) Helicity distribution (no χ^2 cuts)

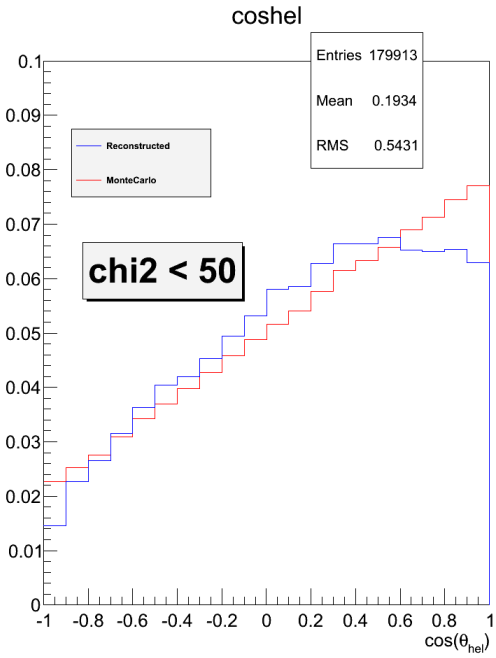

(v) Helicity distribution ($\chi^2 < 50$)

Figure 3.19: χ^2 analysis for A_{FB} and helicity angle ($e^-_R e^+_L$)

3.10 Results

We have 4 quantities to extract the 4 F_1 form factors: The cross section and the helicity angle distribution for each polarisation.

We use a fit to estimate λ_{hel}. To estimate the systematic on λ_{hel} we look for the difference between $\lambda_{hel,reco}$ measured and $\lambda_{hel,MC}$ generated at the parton level. In practice data will be corrected to take into account this difference and therefore we estimate that the residual error will be of order 1/4 the measured difference.

For reconstructed events we have applied $\chi^2 < 50$ in order to avoid the mixing of b-jets. Therefore we take into account the efficiencies after χ^2 cut to calculate statistical errors in reconstructed observables. On the other hand it is not necessary to apply any χ^2 cut for cross sections.

For the cross sections we think that the main source of systematical errors comes from theory and we are currently discussing the matter with theorists. Unless the theory errors are larger than 0.5%, the dominant error comes from the helicity distribution.

Following table shows the expected number of events as a function of the polarisation. We consider an integrated luminosity for each polarisation of $\mathcal{L} = 250\ fb^{-1}$ which will be the real luminosity for ILC.

P(e^-), P(e^+)	σ (fb)	$\mathcal{L}$ (fb^{-1})	$N = \mathcal{L} \times \sigma$
$-100\%, +100\%$	1575	250	393750
$-80\%, +30\%$	964	250	241000
$+100\%, -100\%$	726	250	181500
$+80\%, -30\%$	489	250	122250

Table 3.6: Rescaling factor.

In order to obtain realistic errors with a realistic polarisation we will define the following rescaling factors:

$$f_{LR} = \sqrt{\frac{N(-100\%, +100\%)}{N(-80\%, +30\%)}} = \sqrt{\frac{393750}{251000}} = 1.28$$

$$f_{RL} = \sqrt{\frac{N(+100\%, -100\%)}{N(+80\%, -30\%)}} = \sqrt{\frac{181500}{122250}} = 1.22$$

with these factors we will rescale our statistical errors for fully polarised beams.

3.10.1 Statistical errors

Obs.	MC	Reco	Shift	$(\delta x/x)_{MC}$	$(\delta x/x)_{reco}$	$(\delta x/x)_{MC} \cdot f_{LR}$	$(\delta x/x)_{reco} \cdot f_{LR}$
A_{FB}	0.33	0.303	8.2%	0.43%	0.74%	0.55%	**0.95%**
λ_{hel}	-0.45	-0.49	8.9%	0.59%	0.91%	0.76%	**1.16%**
$\sigma(fb)$	1575	1575	0	0.15%	0.16%	0.19%	**0.20%**

Table 3.7: $e_L^- e_R^+$ polarisation. Large σ.P(e^-) = -100%, P(e^+) = 100%.

Obs.	MC	Reco	Shift	$(\delta x/x)_{MC}$	$(\delta x/x)_{reco}$	$(\delta x/x)_{MC} \cdot f_{RL}$	$(\delta x/x)_{reco} \cdot f_{RL}$
A_{FB}	0.46	0.458	0.43%	0.21%	0.68%	0.26%	**0.83%**
λ_{hel}	0.58	0.53	8.6%	0.67%	1.41%	0.82%	**1.72%**
$\sigma(fb)$	726	726	0	0.24%	0.25%	0.30%	**0.30%**

Table 3.8: $e_R^- e_L^+$ polarisation. Small σ. P(e^-) = 100%, P(e^+) = -100%.

Statistical errors have been calculated by:

$$Shift = \frac{MC - Reco}{MC}, \quad \frac{\delta A_{FB}}{A_{FB}} = \frac{\sqrt{1 - A_{FB}^2}}{A_{FB} \cdot \sqrt{N \cdot \varepsilon}}, \quad \frac{\delta\sigma}{\sigma} = \frac{1}{\sqrt{N \cdot \varepsilon}}, \quad \frac{\delta\lambda_{hel}}{\lambda_{hel}} = \frac{fit\ error}{\lambda_{hel}}$$

where ε is the efficiency of selection of the reconstructed events:

$$\varepsilon = 40\%\ for\ e_L^- e_R^+\ polarisation$$

$$\varepsilon = 45\%\ for\ e_R^- e_L^+\ polarisation$$

These are the efficiencies when we impose $\chi^2 < 50$, they give the total number of reconstructed events. Note that for MC values we use ε=1. In the case of the cross sections (reco) the real efficiencies are $\varepsilon(e_L^- e_R^+) = 88.5\%$ and $\varepsilon(e_R^- e_L^+) = 91.4\%$.

3.10.2 Summary

Following table shows the summary of the results for statistical and systematical errors of λ_{hel} and σ.

P P'	Efficiency	σ (fb)	δσ/σ	eff χ^2	$\delta\lambda_{hel}$ stat	$\delta\lambda_{hel}$ syst	$\lambda_{hel} \pm \delta\lambda_{hel}$
+80% -30%	91.2%	489	0.30%	45.0%	0.97%	1.25%	0.58 ±0.016
-80% +30%	88.4%	964	0.20%	40.0%	0.60%	1.0%	-0.45±0.012

Table 3.9: Final errors of the hadronic side.

Chapter 4

Conclusion

4.1 Couplings LHC vs ILC

With polarized beams, it is possible to measure separately the vector and axial couplings (or equivalently the left and right couplings) of photons and Z in a linear collider at the % level. These results are far better than those quoted in [14] which did not achieve disentanglement. Note also that accuracies on photon coupling are better than for Z couplings.

A significant progress can therefore be achieved towards a more model independent analysis of the top couplings.

These excellent statistical accuracies require:

- outstanding performances from the LC detectors to control reconstructions efficiencies at 0.1% level
- polarization measurements also at the 0.1% level using the WW final state
- understanding QED, QCD and electroweak corrections also at the 0.1% level

In terms of axial and vector accuracies one also obtains accuracies which are far superior to those of [14] as shown by the Table 4.1. These results have been obtained using values from Table 3.9:

Coupling	SM Value	LHC 300 fb-1	e+e- US Study	e+e- this study
ΔF_{1V}^{γ}	-0.66	+0.043 -0.041	+0.047 200 fb-1 -0.047 P=0.8	±0.0025 500 fb-1 P=0.8,0.3
ΔF_{1A}^{γ}	0	+0.051 -0.048	+0.011 100 fb-1 -0.011 P=0.8	±0.0085 id
ΔF_{1V}^{Z}	0.23	+0.34 -0.72	+0.012 200 fb-1 -0.013 P=0.8	±0.005 id
ΔF_{1A}^{Z}	0.59	+.079 -0.091	+.052 200 fb-1 -0.052 P=0.8	±0.019 id

Table 4.1: Coupling errors values for three different studies.

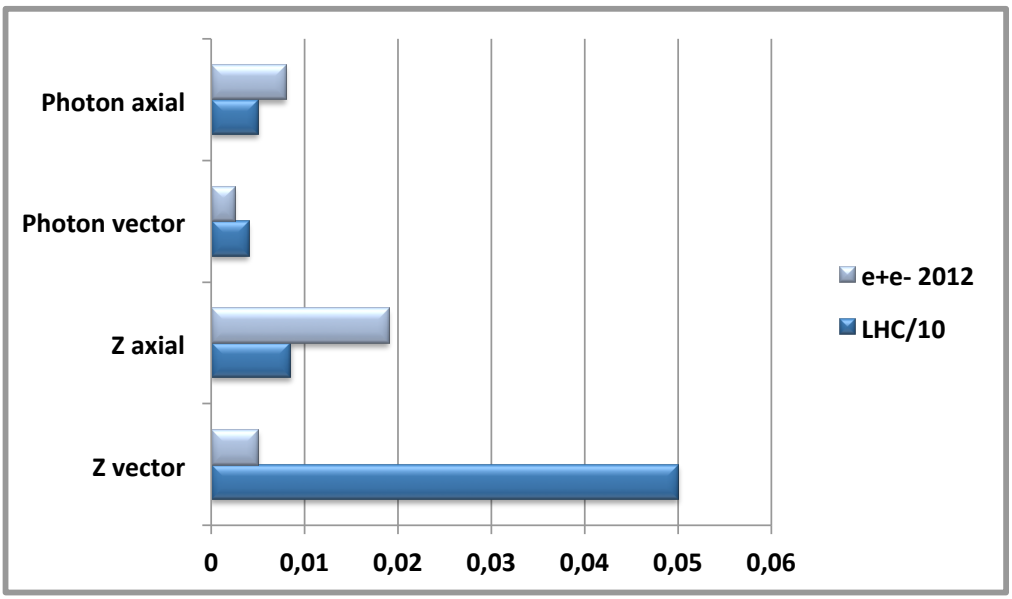

Figure 4.1: Coupling errors for ILC and for LHC.**Note LHC errors are divided by 10.**

The spectacular improvement with respect to LHC errors [14], quoted in Figure 4.1, is not explained by the higher integrated luminosity assumed in the present study but seems to be due to the use of better observables. Comparable accuracies were given for F_1^Z in [14] but without disentanglement with photon couplings.

In the Figure 4.1, LHC errors are compared to the LC results from this analysis.

4.2 Future work

The aim is to repeat this analysis on the hadronic side of the $t\bar{t}$ event in order to combine finally leptonic + hadronic sides and in this way achieve the maximum efficiency and reduce to a negligible amount the wrong reconstructed events. Another goal is recalculating backgrounds ($WW, b \to l$) that probably will vanish.

We expect that LHC analysis will also improve but it will be very hard to compete with LC accuracies on top couplings measurements. LHC will provide precise results on charged currents using top decays and single top production.

These excellent results need to be confirmed by taking better account of possible systematical effects.

Bibliography

[1] PDG July 2012, Standard Model, http://pdg.lbl.gov/

[2] ILC Collaboration, International Linear Collider Reference Design Report. Volume 3: Accelerators, ILC-REPORT-2007-001, August 2007

[3] DBD Physics at the International Linear Collider, draft and outline July 5, 2012, https://www.yousendit.com/download/QlVneFlYTmFBNkVUWThUQw

[4] International Linear, Collider Physics and Detectors, Status Report 2011

[5] J. Fuster, S. Heinemeyer, C. Lacasta, C. Marias, A. Ruiz-Jimeno, M. Vos, http://arxiv.org/pdf/0905.2038.pdf

[6] Philippe Doublet thesis, *Production du quark top à l'International Linear Collider.* 3 october 2011

[7] ATLAS, Physics TDR, ATLAS DETECTOR AND PHYSICS PERFORMANCE, Vol.II, 25 May 1999

[8] A. Moll, A. Raspereza, Max-Plank-Institute for Physics, *Study of Top Quark Pair Production at ILC*

[9] F.Boudjema, B.Mele et al., Standard Model Processes, in: Physics at LEP2, ed. by G.Altarelli, T.Sjostrand, F.Zwirner, CERN report 96-01, vol. I, Geneva, 1996, p. 207-249 (hep-ph/9601224)

[10] J.Fleisher, A.Leike, T.Riemann, A.Werthenbach, hep-ph/0303359, February 2003

[11] S. Agostinelli *et al.* [GEANT4 Collaboration], Nucl. Instrum. Meth. A **506** (2003) 250.

[12] I. Garcia, E.Ros, J.Trenado, M.Vos [DESY-NOTE] LC-REP-2012-003. http://www-flc.desy.de/lcnotes/

[13] M. Martinez and R. Miquel, Eur. Phys. J. C **27** (2003) 49 [hep-ph/0207315].

[14] Report of the 2005 Snowmass top/QCD working group. e-Print: hep-ph/0601112

Aknowledgements

Este trabajo no hubiera sido posible sin Eduardo Ros, mi tutor de Máster y de mi futura tesis doctoral. Sin su exigencia y su ayuda el resultado no hubiera sido tan satisfactorio, me ha hecho ver lo que soy capaz de hacer.

También quiero agredecer la gran aportación de Marcel Vos, mi segundo tutor, por su paciencia cada vez que iba a su despacho una y otra vez. Sin él, todos los programas de análisis no hubieran funcionado tan bien.

Por otro lado quiero expresar mi gratitud a Francois Richard, un gran físico francés con el que he aprendido mucho y siempre he sentido su apoyo. Agradecer a Jeremy Rouenne por facilitarme los datos de la full simulation y a Philipe Doublet porque su tesis doctoral ha sido la base de mi trabajo.

La dedicatoria de este trabajo es claramente para mis padres y mi hermano, gracias a ellos soy la persona que soy y son la razón por la que nunca dejo de luchar.